JOURNAL OF GEOPHYSICAL RESEARCH: PLANETS, VOL. 118, 1323–1349, doi:10.1002/jgre.20092, 2013

Bed thickness distributions on Mars: An orbital perspective

K. M. Stack,[1] J. P. Grotzinger,[1] and R. E. Milliken[2]

Received 5 March 2013; revised 2 May 2013; accepted 3 May 2013; published 20 June 2013.

[1] Studies on Earth show that sedimentary bed thickness and bed thickness distributions record information about the processes controlling sediment deposition. High-resolution digital terrain models (DTMs) such as those derived from the High Resolution Imaging Science Experiment (HiRISE) now provide the opportunity to quantify bed thickness properties on Mars over several orders of magnitude, down to the submeter scale. This study uses HiRISE DTMs and visible images to measure bed thickness distributions at 10 deposits on Mars, with the aim of determining whether statistical techniques can provide useful criteria for distinguishing sedimentary depositional processes. Basic statistics, including mean thickness and range, are examined, as are histograms, cumulative frequency plots, and log-log plots. Statistical tests interrogate these deposits for thinning or thickening upward trends and the presence of normal, lognormal, and exponential distributions. Although there are challenges associated with these methods, the statistical analysis of bed thickness, coupled with morphological and mineralogical interpretations, has the potential to be a powerful tool for characterizing and classifying sedimentary rocks on Mars. In particular, bed thickness statistics are particularly well suited for examining changes in sediment supply and accommodation within Martian sedimentary sequences.

Citation: Stack, K. M., J. P. Grotzinger, and R. E. Milliken (2013), Bed thickness distributions on Mars: An orbital perspective, *J. Geophys. Res. Planets*, *118*, 1323–1349, doi:10.1002/jgre.20092.

1. Introduction

[2] In situ and remote observations of the Martian sedimentary record have shown that bedding is as fundamental a characteristic of sedimentary rocks on Mars as it is on Earth [*Malin and Edgett*, 2000; *Grotzinger and Milliken*, 2012]. Where primary, bedding generally represents a profound attribute of the stratigraphic record: the presence of hiatuses where time is represented by a surface rather than a volume of rock [*Blackwelder and Barrows*, 1911; *Wheeler*, 1958, 1959; *Sloss*, 1963; *Sadler*, 1981; *Christie-Blick and Driscoll*, 1995]. The thinnest beds have the potential to record individual sedimentation events, whereas thicker beds represent the amalgamation of strata that are related by composition (lithostratigraphic units) or time (sequences and cycles) [*Mitchum and Vail*, 1977]. Stratified deposits on Earth provide the principal archive of past surface processes, and widespread stratified outcrops on Mars may hold similar promise [*Tanaka*, 1986; *Malin and Edgett*, 2000; *Grotzinger and Milliken*, 2012].

[3] Mariner 9 images first revealed the existence of sedimentary, layered materials in both the polar [*Murray et al*., 1972; *Soderblom et al*., 1973; *Cutts*, 1973] and mid-latitude regions [*Sharp*, 1973] of Mars. The Viking mission [*Snyder*, 1979], High Resolution Stereo Camera (HRSC) data [*Neukum et al*., 2004], and high-resolution images from the Mars Orbiter Camera (MOC) [*Malin and Edgett*, 2001] and the High Resolution Imaging Science Experiment (HiRISE) [*McEwen et al*., 2010; *Grotzinger and Milliken*, 2012] show these deposits to occur in diverse settings, including impact craters, canyons, channels, and plateaus, reflecting sedimentary origins in aeolian, fluvial, and possibly lacustrine environments [*Scott and* Tanaka, 1986; *Lucchitta et al*., 1992; *Carr*, 1996; *Malin and Edgett*, 2000; *Edgett and Malin*, 2002; *Moore et al*. [2003]; *Squyres et al*., 2004; *Grotzinger et al*., 2005; *Jaumann et al*., 2007; *Grotzinger et al*., 2011]. Recent in situ observations by the Mars Exploration Rovers *Spirit* and *Opportunity* [*Squyres et al*., 2004; *Grotzinger et al*., 2005; *Squyres et al*., 2007] and by the Mars Science Laboratory Curiosity rover [*Grotzinger et al*., 2012] have allowed outcrop-scale geological investigations of these past environments.

[4] Numerous studies suggest a possible link between climate change, orbital parameters, and layered ice-rich deposits in the polar regions of Mars [*Laskar et al*., 2002; *Milkovich and Head*, 2005; *Fishbaugh et al*., 2010a, 2010b, *Limaye et al*., 2012]. In contrast, few studies have attempted quantitative stratigraphic analysis of layering observed in what are likely sediment-dominated deposits [*Lewis et al*., 2008; *Lewis*, 2009; *Cadieux* [2011]; *Fueten et al*., 2011]. *Lewis et al*. [2008, 2010] identified rhythmic bedding in sedimentary deposits of Arabia Terra, Gale crater, Juventae

Additional supporting information may be found in the online version of this article.

[1]Department of Geological and Planetary Sciences, California Institute of Technology, Pasadena, California, USA.
[2]Department of Geological Sciences, Brown University, Providence, Rhode Island, USA.

Corresponding author: K. M. Stack, Department of Geological and Planetary Sciences, California Institute of Technology, Pasadena, CA 91125, USA. (kstack@caltech.edu)

2169-9097/13/10.1002/jgre.20092

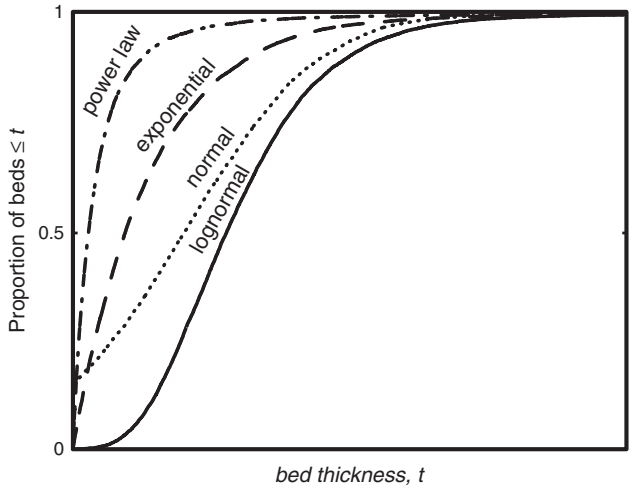

Figure 1. Representative exponential, lognormal, normal, and power-law cumulative bed thickness distributions plotted on a linear scale.

Chasma, and the Medusa Fossae formation, suggesting that periodicity may be related to orbital forcing in the Milankovitch band. However, cyclic bedding is rare among putative sedimentary strata on Mars [*Lewis et al*., 2010; *Grotzinger and Milliken*, 2012], and the search for periodicity is just one way bed thickness can be used to study the stratigraphic record. On Earth, the frequency distribution of sedimentary bed thickness has been related to depositional environment [*Carlson and Grotzinger*, 2001; *Talling*, 2001] and process [*Rothman et al*., 1994; *Beattie and Dade*, 1996]. Furthermore, systematic changes in bed thickness have been linked to basin-scale variations in sediment supply and accommodation [*Fischer*, 1964; *Read and Goldhammer*, 1988]. Despite the successful implementation of statistical bed thickness analyses on Earth and the recent ability to do so at the submeter scale on Mars, the potential to classify deposits and constrain depositional processes using bed thickness has been largely unexplored for Mars.

[5] This study seeks to understand how the statistical analysis of bed thickness can be adapted and applied to sedimentary strata on Mars while working within the constraints and limitations of orbital data sets. Building upon the work of *Lewis et al*. [2008, 2010], this study explores additional ways that bed thickness measurements can provide an objective and quantitative approach for describing and classifying Martian layered deposits. High-resolution images and digital terrain model (DTMs) are used to measure stratal thickness for 10 spatially distinct Martian deposits that likely represent a variety of depositional settings, with special focus on the deposits in Holden crater, Gale crater, and on the plateau west of Juventae Chasma. This study shows that bed thickness measurements, coupled with histograms, cumulative frequency (CF) distributions, and the results of statistical testing can enhance understanding of the processes that control sediment transport and deposition on Mars. As additional HiRISE DTMs become publicly available in future years, the methods presented here can provide a foundation for more detailed studies of bed thickness for sedimentary deposits on Mars whose depositional settings are well constrained, providing even clearer insight into relationships between sedimentary process and bed thickness for Martian strata.

2. Background

2.1. Statistical Analysis of Bed Thickness on Earth

[6] Statistical methods have been used to study the history of deposition in several sedimentary settings on Earth. The frequency distribution of turbidite bed thickness are thought to record information about initial sediment volume and source, flow rheology [*Talling*, 2001], lateral distribution and migration of facies [*Carlson and Grotzinger*, 2001], and intrinsic and extrinsic controls on depositional processes [*Rothman et al*., 1994; *Beattie and Dade*, 1996; *Chen and Hiscott*, 1999]. Terrestrial turbidite frequency distributions are variable, showing truncated Gaussian, lognormal [*Ricci Lucchi*, 1969; *Talling et al*., 2001], exponential [*Drummond and Wilkinson*, 1996], cumulative power-law [*Carlson and Grotzinger*, 2001], and segmented power-law [*Rothman and Grotzinger*, 1995; *Sylvester*, 2007] trends. Bed thickness distributions have also been studied for peritidal carbonates [*Wilkinson et al*., 1997, 1999; *Wilkinson and Drummond*, 2004; *Burgess*, 2008], mixed carbonate-clastic deposits [*Drummond and Wilkinson*, 1996; *Wilkinson and Drummond*, 2004], debris flows [*Rothman and Grotzinger*, 1995], and fluvial deposits [*Atkinson*, 1962]. Still, the majority of studies have preferentially focused on turbidite and carbonate deposits to the extent that the understanding of bed thickness distributions on Earth is not balanced through all depositional environments.

[7] Lognormal, exponential, and power-law statistical distributions are the most commonly observed trends in terrestrial sedimentary sequences (Figure 1), and these are described in detail below.

2.1.1. Lognormal

[8] A data set whose logarithm follows a normal distribution is lognormally distributed. Lognormal distributions arise when a variable is the product of a number of independent random variables rather than the addition of these variables, as for a normal distribution [*Davis*, 2002].

[9] Lognormal distributions are common in geological data sets [*Koch and Link*, 1980], and sedimentary sequences on Earth commonly exhibit lognormal distributions [*Hinnov and Goldhammer*, 1991; *Drummond and Wilkinson*, 1996; *Talling*, 2001]. *Atkinson* [1962] attributes lognormal trends observed in fluvial sandstones, shales, and conglomerates to lognormally distributed time intervals between flood events and movements along faults. *Talling* [2001] suggests that the observed lognormal distribution of turbidite beds is a primary signal resulting from the multiplicative addition of several randomly distributed parameters, such as flow duration, turbulence, and settling velocity — all of which are processes known to contribute to the thickness of any given turbidite bed. Despite the prevalence of lognormal trends in sedimentary rocks, such distributions remain first and foremost an empirical explanation for the observed distribution of bed thickness. Accordingly, *Drummond and Wilkinson* [1996] suggest that lognormal trends result from a sampling bias in which the thinnest beds of exponential distributions are missed during counting.

Table 1. HiRISE DTMs and Orthoimages Used in This Study

DTMs	Resolution of Stereo Pairs (m/pixel)	Emission Angles	Roll Angles of Stereo Pairs	Precision of Elevation Values in DEM (m)	Grid Spacing of DTM	Resolution of Ortho-image (m/pixel)
DTEEC_019045_1530_019322_1530_U01	0.263	9.4	8.877	0.09	1 m	25 cm, 1 m
	0.278	21.6	−19.865			
DTEEC_002088_1530_002154_1530_U01	0.265-0.530	12.2	11.406	0.24	1 m	25 cm, 1 m
	0.528	11.1	−10.871			
DTEEC_015999_1535_016276_1535_U01	0.269	14.9	13.941	0.09	1 m	25 cm, 1 m
	0.266	14.9	−13.673			
DTEEC_003434_1755_003579_1755_U01	0.262	1.1	1.003	0.17	1 m	25 cm, 1 m
	0.274	17.9	16.629			
DTEEC_012551_1750_012841_1750_U01	0.271	3.5	−3.158	0.09	1 m	25 cm, 1 m
	0.301	27.7	25.598			
DTEEC_001488_1750_001752_1750_U01	0.267	2.5	2.365	0.15	1 m	25 cm, 1 m
	0.28	17.5	−16.165			
DTEEC_019698_1750_019988_1750_U01	0.291	24.1	−22.115	0.07	1 m	25 cm, 1 m
	0.278	14.7	13.722			
DTEEC_003816_1245_004106_124_A01	0.254	4.1	3.823	0.14	1 m	25 cm, 1 m
	0.275	23.6	21.868			
DTEEC_002661_1895_003294_1895_U01	0.296	21.8	20.111	0.19	1 m	25 cm, 1 m
	0.278	4.8	4.428			
DTEEC_001546_2015_001955_2015_U01	0.284	2.8	2.474	0.35	1 m	25 cm, 1 m
	0.287	6.4	−5.938			
DTEEC_001918_1735_001984_1735_U01	0.285	23.9	22.048	0.12	1 m	25 cm, 1 m
	0.262	0.8	−0.763			
DTEEC_010228_1490_016320_1490_A01	0.258	8.1	−7.452	0.13	1 m	25 cm, 1 m
	0.26	13.5	12.703			
DTEEC_002878_1880_002733_1880_U01	0.279	9.3	8.587	0.18	1 m	25 cm, 1 m
	0.278	7.6	−6.996			
DTEEC_019757_1560_020034_1560_U01	0.262	8.2	7.746	0.11	1 m	25 cm, 1 m
	0.272	17.8	−16.373			

2.1.2. Exponential

[10] The recurrence intervals of a Poissonian stream of events are approximated in the continuous limit by an exponential distribution. The presence of an exponential distribution in a series of strata suggests the operation of a stochastic Poisson process where the deposition duration of a particular unit, which is assumed to be proportional to the unit thickness, is random and unrelated to the onset or duration of deposition of the next unit [*Burgess*, 2008]. An exponential frequency distribution of bed thickness takes the form

$$N(t) = ae^{(-bt)} \tag{1}$$

where N is the number of beds of thickness t and a and b are constants.

[11] Exponential thickness distributions have been observed in turbidite deposits and numerous ancient carbonate deposits [*Wilkinson et al*., 1997, 1999; *Burgess*, 2008]. *Drummond and Wilkinson* [1996] suggest that both carbonate and clastic sedimentary sequences follow an exponential distribution where the number of thin beds is much greater than the number of thick beds, frequency decreases at a particular rate as thickness increases, and there is no modal thickness. The exponential model invokes a stochastic, memory-less stacking pattern at odds with deposition driven by cyclic or periodic forcing mechanisms [*Drummond and Wilkinson*, 1996; *Burgess*, 2008]. As a result, a stratigraphic sequence may only exhibit the effects of external forcing mechanisms (i.e., sea-level oscillations) on a multidecameter scale [*Wilkinson et al*., 1997, 1999; *Wilkinson and Drummond*, 2004; *Burgess*, 2008]. The exponential distribution of bed thickness is supported by the common occurrence of exponential processes in nature and the likely unavoidable bias against thin beds that occurs when tabulating stratigraphic subdivisions [*Drummond and Wilkinson*, 1996].

2.1.3. Power law

[12] Scale-invariant power-law relationships can also describe the distribution of sedimentary bed thickness [*Rothman and Grotzinger*, 1995; *Awadallah et al*., 2001; *Carlson and Grotzinger*, 2001]. The equation for a power-law relationship takes the form

$$N(t) = ct^{(-d)} \tag{2}$$

where t is bed thickness, N is the number of beds of thickness t, c is a constant, and d is a constant scaling exponent given by the slope of the plot in log(N) versus log(t) space. For data sets exhibiting power-law scaling, the exponent d is related to depositional variations such as basin geometry or flow types [*Rothman et al*., 1994; *Rothman and Grotzinger*, 1995]. Numerous studies have documented power-law distributions of bed thicknesses in turbidite sequences, but the cause of this observed power-law trend is debated. *Rothman et al*. [1994] suggest that the distribution of turbidite bed thickness represents a self-organized system regulated by a complex nonlinear diffusion equation that exhibits power-law scaling, while *Beattie and Dade* [1996] and *Awadallah et al*. [2001] favor turbidite deposition driven by the external forcing of earthquakes that follow Gutenberg-Richter scaling — another power law.

[13] Following the assumption that bed thickness frequency follows a power law, systematic deviations from expected power-law behavior have been interpreted to have process significance. *Carlson and Grotzinger* [2001] link deviations from power-law behavior to erosion, amalgamation,

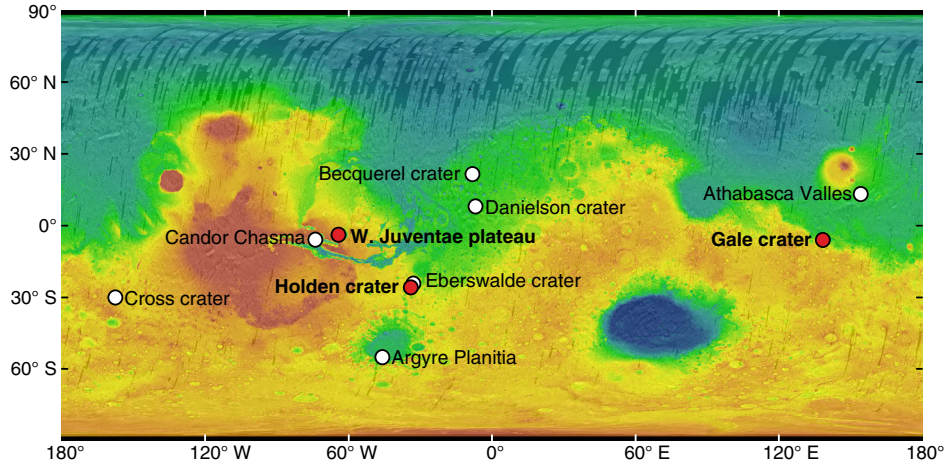

Figure 2. Reference map showing locations discussed in this paper. Sites where multiple bed thickness distributions were measured are highlighted in red. Basemap is MOLA topography draped over a THEMIS Day IR mosaic.

and channelization, thereby using bed thickness distributions to distinguish between proximal and distal facies within submarine fan deposits. *Carlson and Grotzinger* [2001] also show that the process of bed amalgamation can create a lognormal distribution from a power-law distribution. If correct, this is a powerful concept suggesting that any given depositional system may behave as a filter capable of regulating bed thickness and, by implication, bed volumes [*Jerolmack and Paola*, 2010].

[14] Alternatively, segmented power laws have been invoked to describe deviations of natural bed thickness data from power-law behavior at very small or large thicknesses [*Rothman and Grotzinger*, 1995; *Malinverno*, 1997]. *Malinverno* [1997] suggests that bed thickness data should plot as a segmented power law described by linear trends of different slope if there is a relationship between bed length and thickness that depends on bed volume.

[15] Although a variety of distributions have been invoked to describe sedimentary bed thickness on Earth and the meaning of these distributions is actively debated, most studies agree that bed thickness distributions can provide meaningful insight into the magnitude, duration, and recurrence of depositional events. In some cases, bed thickness distributions can even be linked directly to specific depositional environments. For these reasons, statistical analysis of bed thickness is especially compelling on Mars, where the methods and data available to study sedimentary sequences are limited.

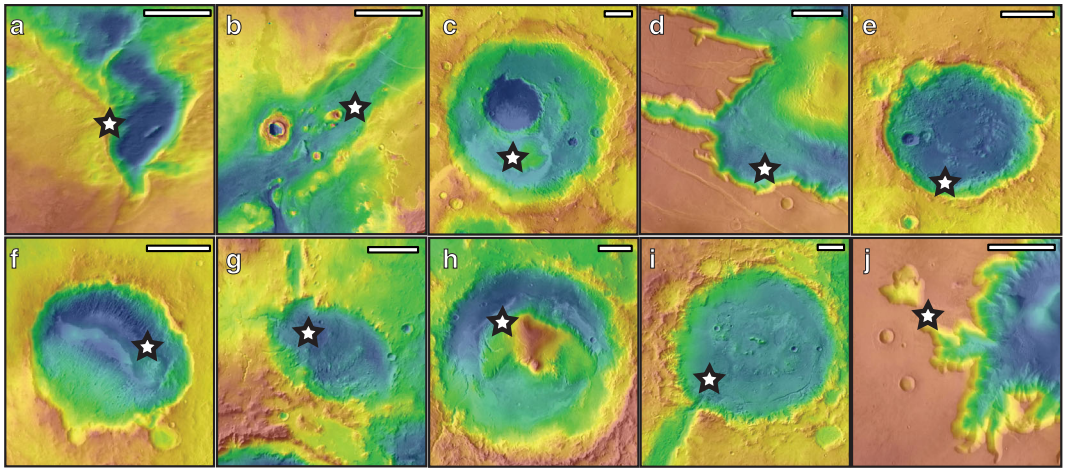

Figure 3. Geomorphic context of deposits examined in this study. Stars indicate the location of measured sections on MOLA topography draped over a THEMIS Day IR mosaic. (a) Argyre Planitia: −55.2 N, 314.3 E. (b) Athabasca Valles: 9.6 N, 156.3 E. (c) Becquerel crater: 21.4 N, 351.9 E. (d) Candor Chasma: −6.5 N, 283.1 E. (e) Cross crater: −30.6 N, 202.2 E. (f) Danielson crater: 8.12 N, 353.1 E. (g) Eberswalde crater: −23.9 N, 326.5 E. (h) Gale crater: −4.8 N, 137.4 E. (i) Holden crater: −26.6 N, 325.2 E. (j) Plateau west of Juventae Chasma: −4.7 N, 296.4 E. Scale bar = 25 km.

Table 2. Study Sites

Study Site	Setting	Orbital Facies [i.e., *Grotzinger and Milliken*, 2012]	Selected References
Holden Crater	Crater interior	Distributary Network	*Pondrelli et al*. [2005]; *Grant et al*. [2008]; *Milliken and Bish* [2010]; *Grant et al*. [2011]
W. Juventae Plateau	Interchasm/ intercrater plains	Laterally Continuous Heterolithic Strata	*Milliken et al*. [2008]; *Bishop et al*. [2009]; *Weitz et al*. [2008, 2010]; *Le Deit et al*. [2010]
Gale Crater	Crater interior	Laterally Continuous Sulfate Strata	*Malin and Edgett* [2000]; *Anderson and Bell* [2010]; *Milliken et al*. [2010]; *Thomson et al*. [2011]
Argyre Planitia	Impact basin interior	-	*Howard* [1981]; *Parker et al*. [1986]; *Kargel and Strom* [1992]; *Hiesinger and Head* [2002]; *Banks et al*. [2009]
Athabasca Valles	Outflow channel	-	*Rice et al*. [2003]; *Burr* [2003, 2005]; *Leverington* [2004]; *Jaeger et al*. [2007, 2010]
Becquerel Crater	Crater interior	Rhythmite	*Lewis et al*. [2008]; *Cadieux* [2011]
Candor Chasma	Chasm	Laterally Continuous Sulfate Strata	*Okubo and McEwen* [2007]; *Fueten et al*. [2008]; *Murchie et al*. [2009] *Metz et al*. [2010]; *Okubo* [2010]
Cross Crater	Crater interior	Laterally Continuous Heterolithic Strata	*Wray et al*. [2011]
Danielson Crater	Crater interior	Rythmite/Laterally Continuous Sulfate Strata	*Edgett and Malin* [2002]; *Edgett* [2005]; *Cadieux* [2011]
Eberswalde Crater	Crater interior	Distributary Network	*Bhattacharya et al*. [2005]; *Lewis and Aharonson* [2006]; *Pondrelli et al*. [2008]

3. Methods

3.1. Identifying Beds From Orbit on Mars

[16] This study defines a sedimentary bed as the thinnest recognizable unit observable in orthorectified HiRISE images. Generally, an individual bed is identified as an observable change in image brightness that is laterally continuous for tens of meters or more or where a distinct shelf-like topographic expression is observed. Little else is known about the reason for stratification. It is important to consider that bedding likely exists at finer scales than is resolvable in HiRISE imagery. For example, in situ observations of bedding at the *Opportunity* landing site (i.e., *Grotzinger et al*. [2005]) revealed stratification on a scale not observable in the orbital data. However, it is assumed that the submeter-scale to meter-scale bedding observable in HiRISE images has sedimentary depositional significance [i.e., *Lang et al*., 1987; *Sgavetti et al*., 1995], meaning that it is not due to secondary processes such as diagenetic overprinting or metamorphism, including hydrothermal alteration. It is recognized though that if such processes produce boundaries parallel with true bedding, these boundaries will be indistinguishable from that bedding in orbital data.

3.2. Orbital Data

[17] Table 1 lists the HiRISE DTMs used to measure bed thickness in this study. The U.S. Geological Survey generated DTMs according to the methods of *Kirk et al*. [2008]. The DTMs have grid spacings of 1 m and absolute elevations tied to data acquired by the Mars Orbiter Laser Altimeter (MOLA; *Smith et al*. [2001]). The expected precision (EP) of the vertical elevation values extracted from the DTMs (Table 1) was calculated using the equation of *Kirk et al*. [2008], which takes into account the viewing geometry and resolution of the HiRISE imagery used to create the DTM,

$$\mathrm{EP} = \rho \times \mathrm{GSD}/(P/h) \tag{3}$$

where ρ is the pixel matching error assumed to be (1/5), GSD is the ground sample distance or the meter/pixel resolution of the more oblique image in the HiRISE stereo pair, and P/h is the ratio of parallax to height. For a narrow angle camera such as HiRISE, this is equal to

$$P/h = |\tan(e_1) \pm \tan(e_2)| \tag{4}$$

where e_1 and e_2 are the emission angles of the HiRISE stereo pair and the sign of the equation depends on whether the stereo pairs are viewing the target from the same side (−, roll angles are of the same sign) or opposite sides (+, roll angles are of opposite signs). For the DTMs listed in Table 1, the vertical precision is estimated to be between 0.07 and 0.35 m, with all but two DTMs having a vertical precision better than 0.20 m.

[18] HiRISE images orthorectified to the corresponding DTM [*Kirk et al*., 2008] were used to measure bedding orientation and bed thickness. Beds were measured at each location using both the 25 cm/pixel and 1 m/pixel orthoimages so that the effects of image resolution on bed thickness measurements and statistical results could be examined.

3.3. Measuring Bed Thickness

3.3.1. Measured Sections

[19] Bed thickness was measured in Holden crater, on the plateau west of Juventae Chasma, in Gale crater, Argyre Planitia, Athabasca Valles, Becquerel crater, Candor Chasma, Cross crater, Danielson crater, and Eberswalde crater (Figures 2 and 3 and Table 2). Although the selection of study sites was determined by the availability of high-resolution DTMs produced by the U.S. Geological Survey, the chosen sites fortuitously represent a variety of depositional settings and styles (Table 2).

[20] Multiple approximately correlative sections were measured in Holden crater, on the plateau west of Juventae Chasma, and in the lower strata of Mt. Sharp in Gale crater (Figures 4–6). In Holden crater, bed thickness distributions were measured at 10 continuous vertical sections in the interval identified by *Grant et al*. [2008] as the lower unit and by *Pondrelli et al*. [2005] as Sed Unit 1. The measured sections in Holden crater were spaced along ~17 km of outcrop and arranged at increasing distance from the rim of the crater such that H1 is closest to the rim, H10 is farthest from the rim, and the remaining sections are located along a line between H1

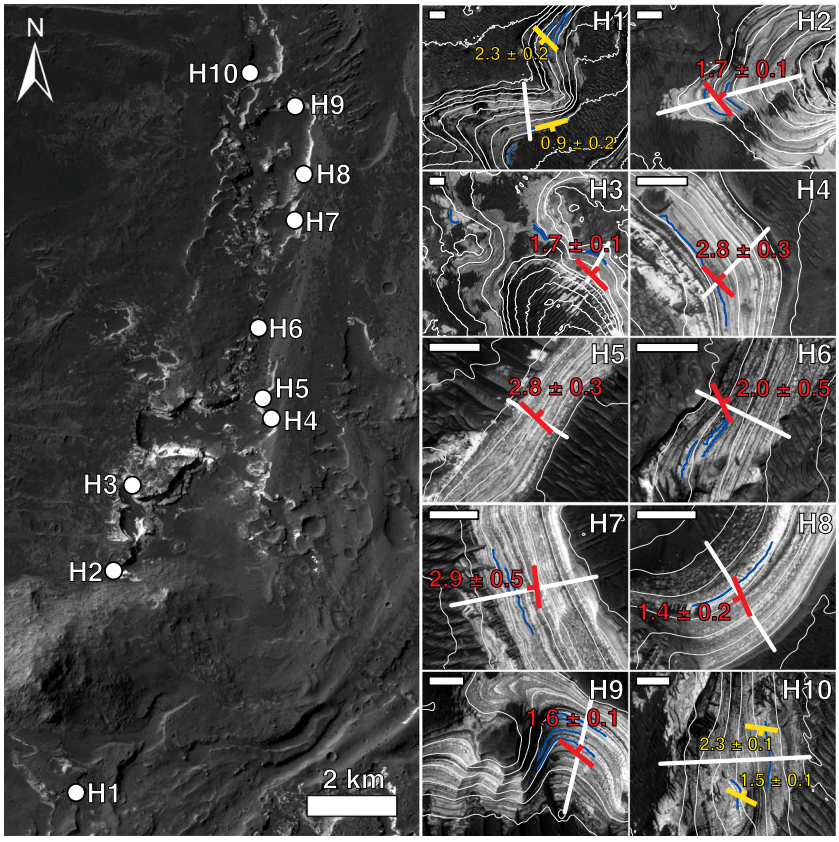

Figure 4. (Left) Location of Holden sections H1-H10 plotted on CTX image P22_009696_1531_XI_26S034W_080821. (Right) Sections along which bed thickness was measured. H1: HiRISE ESP_019045_1530; H2-H9: PSP_002088_1530; H10: ESP_015999_1535. Blue traces indicate profiles along which coordinates were extracted for orientation measurements. Orientation measurements displayed in red represent average strike and dip for each section; measurements displayed in yellow are representative individual measurements for sections whose beds were assumed to be horizontal. All individual orientation measurements are listed in Table A1. Scale bar for inset boxes = 50 m; contours = 5 m.

and H10 (Figures 3i and 4). These sections were chosen based on the quality of exposure and the vertical completeness of each section. Due to changes in illumination conditions caused by local changes in topography, it was difficult to correlate the individual Holden sections layer by layer, especially for those spaced farther apart. However, because the sections are all within or underlie the same alluvial fan system, they likely sample the same approximate stratigraphic interval.

[21] The 10 sections measured on the plateau west of Juventae Chasma are spaced ~1 km apart along a 10 km sinuous exposure exposed along the walls of a deep pit 20 km west of Juventae Chasma (Figures 3j and 5). WJ1 is the easternmost section; subsequent sections follow the trace of the outcrop to the northwest (Figure 5). It is possible to trace several beds throughout all of the sections; thus, each section samples the same approximate stratigraphic interval.

[22] Eight sections were measured at the base of Mt. Sharp in Gale crater (Figures 3h and 6). *Milliken et al*. [2010] identified three members within the Lower formation of Mt. Sharp, with a lower member characterized by bright beds, a middle member containing dark-toned strata, and an upper member defined at its base by a dark and smooth marker bed. In this study, two sections were measured in the lower member, three sections in the middle member, and three sections in the upper member (Figure 6). The sections were chosen according to these stratigraphic boundaries so that changes in bed thickness could be examined laterally within the same stratigraphic interval and vertically through the stratigraphy of the Lower formation.

[23] In addition to these three primary localities, bed thickness was also measured at seven other locations on Mars (Figures 3 and 7). Only one section (or two in the case of Candor) was measured at each of these additional locations. One section is located on the eastern flank of a north-south trending sinuous ridge located in the southern portion of the Argyre impact basin (Figures 3a and 7a). The Athabasca section is measured on the southeastern facing flank of a teardrop-shaped landform extending from a small impact crater within Athabasca Valles (Figures 3b and 7b). The section measured in Becquerel crater spans the rhythmic beds previously described by *Lewis et al*., [2008] and *Cadieux* [2011], exposed in a small mound in the southern part of the crater (Figures 3c and 7c). Strata in the southwest region of Candor Chasma are extensively folded and faulted [*Okubo and McEwen*, 2007; *Fueten et al*. 2008; *Metz et al*. [2010];

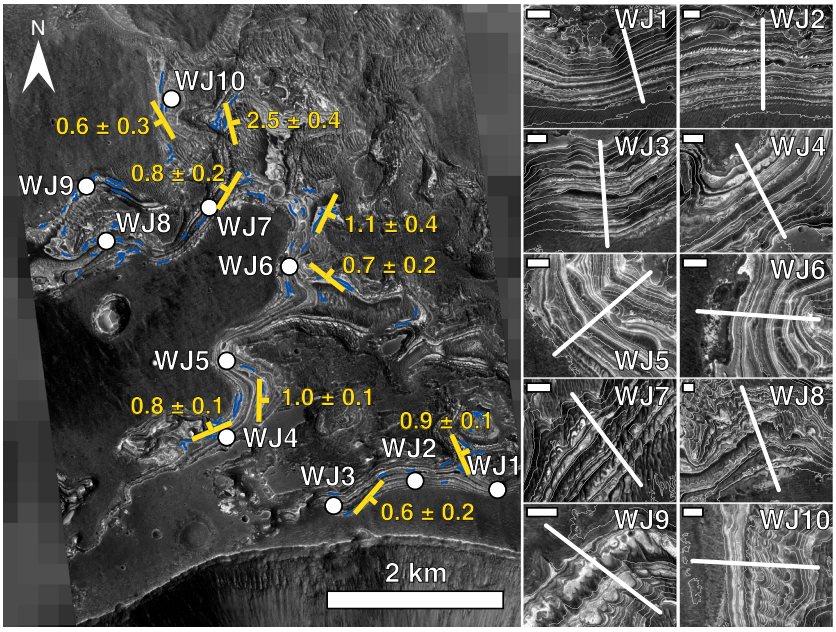

Figure 5. (Left) Location of the sections measured on the plateau west of Juventae Chasma. WJ1-WJ10: HiRISE PSP_003579_1755. Blue traces indicate profiles along which coordinates were extracted for orientation measurements. Orientation measurements displayed in yellow are representative individual measurements since beds were assumed to be horizontal. All individual orientation measurements are listed in Table A1. (Right) Profiles along which bed thickness was measured. Scale bar for inset boxes = 75 m; contours = 5 m.

Okubo, 2010], but the two sections measured here span a short sequence of undisrupted strata (Figures 3d, 7d, and 7e). The measured section in Cross crater spans strata in a terrace that rings the inner rim of the crater (Figures 3e and 7f). The Danielson section spans a portion of layered fill within Danielson crater in Meridiani Planum (Figures 3f and 7g), while the section in Eberswalde crater measures strata exposed in an eroded scarp at the distal edge of a delta (Figures 3g and 7h).

3.3.2. Bed Orientation

[24] The first step in calculating bed thickness was determining the three-dimensional orientation, or strike and dip, of bedding at each outcrop (Figure 8). *X*, *Y*, and *Z* coordinates, where *X* is the easting, *Y* is the northing, and *Z* is the elevation, were extracted from HiRISE DTMs along bedding planes in ArcGIS and fit to a plane using least-squares multiple linear regression in MATLAB [*Lewis et al*., 2008; *Metz*, 2010; *Watters et al*., 2011] (Figures 8b and 8c). A Monte Carlo simulation of the random residual error in the elevation (*Z* coordinate) was performed to obtain the strike, dip, and estimates of error in strike and dip measurements for each bedding plane (Table A1). Multiple orientation measurements were made throughout each section and averaged to obtain one representative orientation measurement for each section (Table A1). If a significant change in orientation was observed within a section, the average strike and dip was used for the appropriate stratigraphic interval.

[25] Orientation measurements obtained from the plateau west of Juventae, Athabasca, Eberswalde crater, and sections H1 and H10 in Holden crater showed shallow dips and inconsistent strike measurements with large errors (Table A1). Therefore, the beds at these locations were assumed to be approximately horizontal.

3.3.3. Correction for True Thickness

[26] For each measured section, a topographic profile running perpendicular to the strike of the outcrop was extracted from the DTM (Figure 8b). The upper and lower boundaries of each bed along the topographic profile were identified by visual inspection of the HiRISE orthoimage using distinct changes in brightness and, when possible, the topographic expression of strata (Figure 8b). Considering the DTM as a continuous surface with interpolated values between the 1 m tiepoints, coordinates (*X*, *Y*, *Z)* of the upper and lower boundaries of each bed in the section were extracted from the DTM using bilinear interpolation in ArcGIS. The apparent thickness of each bed in the measured section was corrected following the procedure of *Groshong* [1999], taking into account the horizontal distance between the upper and lower boundaries of the bed, the change in elevation between the boundaries of the bed, and the strike and dip for the section (Figures 8b and 8d). When the dip of the bed and the topographic slope are in the same direction, the true thickness is described by

$$t = |h\cos\alpha\sin\delta - v\cos\delta| \tag{5}$$

[27] When the dip of the bed and the topographic slope are in opposite directions,

$$t = h\cos\alpha\sin\delta + v\cos\delta \tag{6}$$

where t is true thickness, h is the horizontal distance along the measured section line between the upper and lower bed boundaries, α is the angle between the measured section and the dip direction (Figure 8d), δ is the true dip, and v is the elevation difference between the upper and lower boundaries of each bed (Figure 8b). By applying these corrections to each bed in the

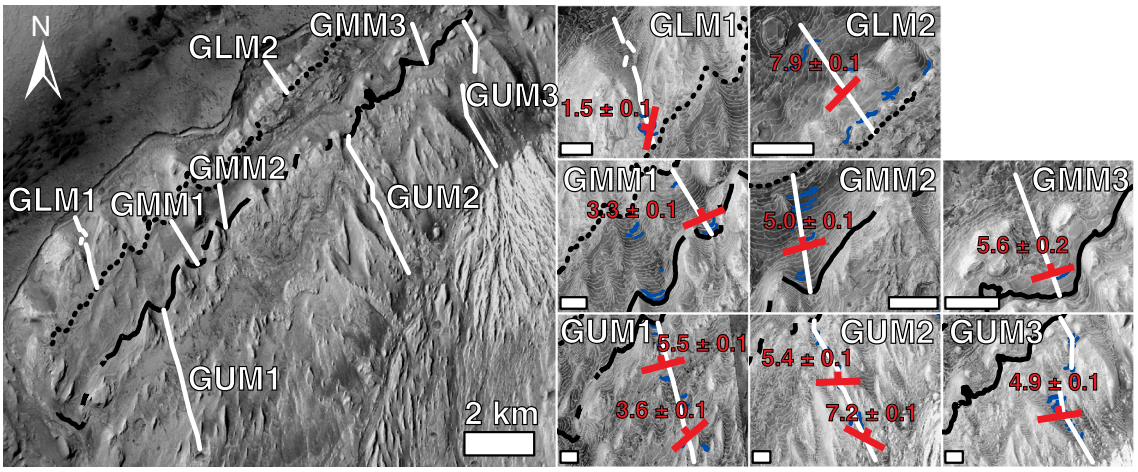

Figure 6. (Left) Sections measured in lower Mt. Sharp, Gale crater on CTX P02_001752_1753_XI_04S222W_061210. Dotted line represents the contact between the lower and middle members; black solid line traces the marker bed between the middle and upper members of the Lower formation. (Right) Profiles along which bed thickness was measured. GLM1, GMM1, GUM1: ESP_012551_1750; GLM2, GMM2: PSP_001488_1750; GMM3, GUM2, GUM3: ESP_019698_1750. Blue traces indicate profiles along which coordinates were extracted for orientation measurements. Orientation measurements displayed in red represent average strike and dip for each section. All individual orientation measurements are listed in Table A1. Scale bar = 500 m; contours = 10m.

measured section, a continuous series of true bed thicknesses from stratigraphic bottom to top was obtained (Figures 9–12).

3.3.4. Error of Bed Thickness Measurements

[28] Absolute errors were calculated for each bed thickness measurement according to equation (A17) (Supporting Information), which propagates errors associated with the DTMs and bed orientation measurements through equations (5) and (6). One-sigma confidence limits for each strike and dip measurement were calculated via the methods of *Metz* [2010] and are reported in Table A1. By averaging strike and dip measurements at each location, errors of the average orientation measurement were greatly minimized. The DTM vertical precision (Table 1) was used to calculate the error of v, while the DTM horizontal resolution (1 m) was used to calculate the error of h. The complete derivation of error propagation for thickness measurements is included in the Supporting Information.

3.4. Statistical Methods

[29] Changes in bed thickness with bed number (sequential beds numbered within the stratigraphic section from bottom to top) for each section are presented in Figures 9–12.

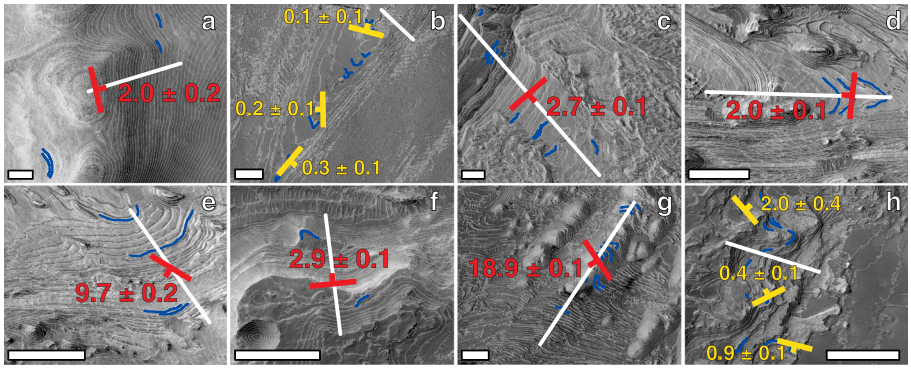

Figure 7. Profiles measured at (a) Argyre Planitia, PSP_003816_1245; (b) Athabasca Valles, PSP_002661_1895; (c) Becquerel crater, PSP_001546_2015; (d) Candor1, PSP_001918_1735; (e) Candor2, PSP_001918_1735; (f) Cross crater, ESP_010228_1490; (g) Danielson crater, PSP_002878_1880; (h) Eberswalde crater, ESP_019757_1560. Blue traces indicate profiles along which coordinates were extracted for orientation measurements. Orientation measurements displayed in red represent average strike and dip for each section; measurements displayed in yellow are representative individual measurements for sections whose beds were assumed to be horizontal. All individual orientation measurements are listed in Table A1. Scale bar = 500 m; contours = 5 m for Athabasca, Cross, and Eberswalde sections; contours = 10 m for Argyre, Becquerel, Candor1, Candor2, and Danielson sections.

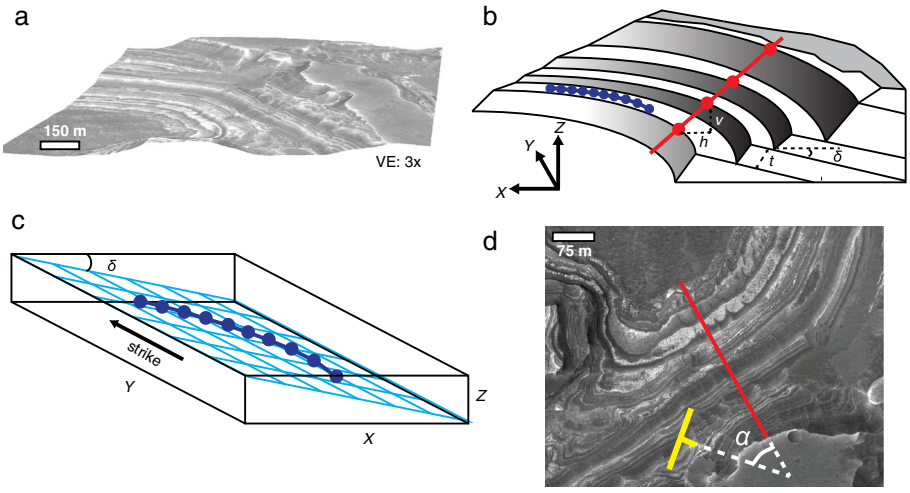

Figure 8. (a) Three-dimensional perspective of sample outcrop (WJ4) from the plateau west of Juventae Chasma. (b) Schematic diagram showing the profile along which bed boundaries were measured (shown in red), points extracted along the bedding plane used to measure the orientation of bedding (shown in blue), and variables used to calculate true bed thickness. (c) Schematic representation of bedding plane points fit to a plane. (d) Plan view of outcrop illustrating α, the angle between the measured profile and the dip direction.

These plots provide an objective way to track systematic changes in bed thickness throughout the section [*Lowey*, 1992]. Bed thickness data were analyzed for overall trends in thinning or thickening using several methods. First, thickness measurements were modeled as a function of stratigraphic position using linear regression. The observed significance probability p from a two-sided t-test was used to reject or fail to reject the null hypothesis that the slope of the model fit was zero. For $p < 0.05$, the null hypothesis was rejected, suggesting that the model slope was statistically significant and nonzero. These cases imply an overall thickening or thinning trend upsection.

[30] Two varieties of runs tests were performed using MATLAB to verify whether successive increases or decreases in bed thickness throughout the sections were random [*Davis*, 2002]. The first test evaluates the null hypothesis that bed thickness values occur in random order and is based on the number of runs above or below the mean bed thickness for each section (RAM, runs about the mean). The second runs test interrogates the null hypothesis that the number of runs up or down is that expected from a random distribution of bed thicknesses (RUD, runs up down).

[31] Bed thickness measurements were plotted in histograms where the frequency of bed thickness is normalized so that the total area in the histogram sums to 1 (Figure 13). This graphical representation provides an approximation of the probability distribution of bed thickness at each location. The number of bins was specified to be 15 for all sections.

[32] To assess whether bed thickness distributions measured at each location followed the expected trend of a normal, lognormal, or exponential distribution, the empirical frequency of bed thickness was plotted together with theoretical distributions on normalized CF plots (Figure 14). Maximum likelihood estimation (MLE) in MATLAB was used to estimate the parameters of normal, lognormal, and exponential distributions for each section using the measured thickness data. Estimated MLE parameters for the normal and lognormal distributions included the mean and standard deviation; for the exponential distribution, the estimated parameter was the mean. The theoretical normal, lognormal, and exponential distributions were then plotted using these parameters (Figure 14).

[33] A Lilliefors test was executed in MATLAB to determine whether empirical bed thickness measurements could be described by normal, lognormal, or exponential distributions. The Lilliefors test is a two-sided Kolmogorov-Smirnov test that does not require a fully specified null distribution [*Lilliefors*, 1967]. This test is suitable when parameters must be estimated from the data, as is the case for the bed thickness measurements here. The test statistic for the Lilliefors test is the same as that for the Kolmogorov-Smirnov test:

$$\mathrm{KS} = \max_{x} |\mathrm{SCDF}(x) - \mathrm{CDF}(x)| \tag{7}$$

where SCDF(x) is the empirical cumulative distribution function (CDF) measured from the sample and CDF(x) is the CDF of a distribution with the same parameters (e.g., mean and standard deviation) as the sample. The Lilliefors test considers the maximum discrepancy between the empirical CDF and the theoretical CDF, where significance probability, p, is the probability of such an extreme discrepancy occurring by chance if the data followed the specified distribution. If the most extreme discrepancy has a probability of occurring at a significance probability <0.05, the null hypothesis that the distribution is a good fit for the data was rejected. This analysis used the Lilliefors test because this test is valid for small sample sizes and does not require that data be grouped into arbitrary categories, as for the χ^2 goodness-of-fit test [*Davis*, 2002]. In addition, this test is valid for the location-scale family of probability distributions, including normal, lognormal, and exponential distributions [*Lilliefors*, 1967, 1969].

[34] To examine the possibility of power-law trends in the data, which may indicate a relationship with scale-invariant processes common in nature, thickness data were also plotted on log-log probability plots (Figure 15). If a data set exhibits

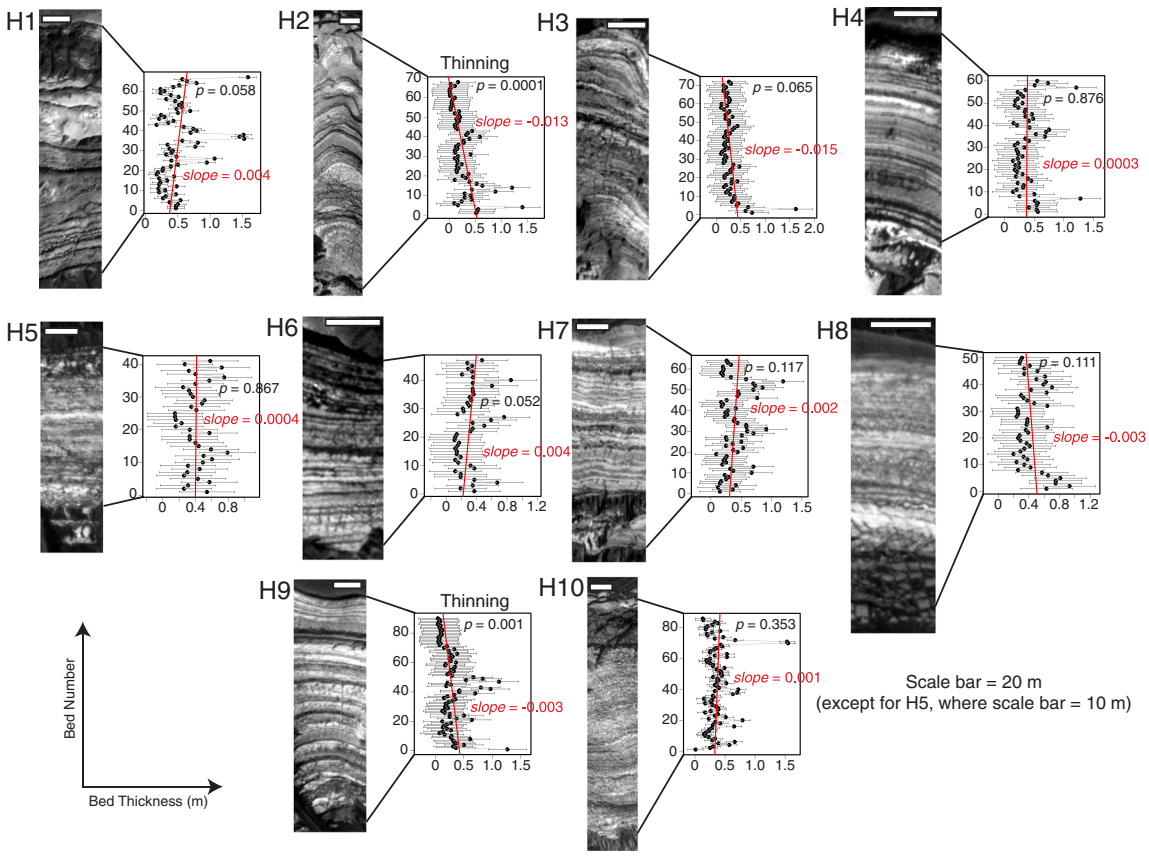

Figure 9. Bed thickness displayed as a function of stratigraphic position for sections measured in Holden crater. Slope values (bed thickness/bed number) are displayed in red. For p less than 0.05, the null hypothesis is rejected and the section is assigned a thinning of thickening trend. Scale bar = 20 m.

power-law behavior, it will plot as a linear function in log-log space.

4. Results

4.1. Holden Crater

4.1.1. Bed Thickness Statistics

[35] Table 3 lists the total section thickness, total number of beds n, range of bed thickness, mean bed thickness μ, and standard deviation σ, measured with the 25 cm/pixel and 1 m/pixel orthoimages for each section. Total thickness for Holden sections ranges between ~15 and 35 m. The number of beds measured using the 25 cm/pixel orthoimages ranges from 41 beds (H5) to as many as 90 beds (H9), and the mean bed thickness ranges from 0.26 m (H2) to 0.51 m (H1). Using the 1 m/pixel orthoimages (Table 3), the number of beds is approximately half that measured with the 25 cm/pixel orthoimages, ranging from 23 beds (H5) to only 49 beds (H9). Mean bed thickness approximately doubles when beds were identified with the lower resolution orthoimages, ranging from 0.36 m (H2) to 0.92 m (H1). The maximum bed thickness measured with the 25 cm orthoimage was 1.62 m (H3). In contrast, the thickest bed measured with the 1 m orthoimage was almost three times higher (4.51 m, H1).

[36] Error bars estimated for Holden thicknesses measurements are strongly influenced by the vertical precision of the DTMs. The H1 and H10 sections were measured using a DTM with a high vertical precision, so the estimated error of the measurements is smaller compared to the error of measurements in H2-H9, which were measured using a DTM with a lower vertical precision (Table 1).

4.1.2. Trends in Thickness Versus Stratigraphic Position

[37] Eight of ten Holden sections show no statistically significant thinning or thickening upward trends when beds were identified with the 25 cm/pixel orthoimage (Figure 9). Only H2 and H9 show trends, both thinning upward, although the estimated error bars on individual measurements in these sections are large enough to cover nearly the full range of measured thicknesses (Figure 9). Using the 1 m orthoimage, 4 of the 10 sections show no thinning or thickening trends (H3-H5, H7), whereas 4 sections show thickening upward trends and 2 thinning upward trends (Table A2).

[38] Significance testing for RAM using the 25 cm/pixel orthoimage thickness data reveals that 8 of 10 sections are consistent with nonrandom ordering of deviations above and below the mean (Table 4). In contrast, the null hypothesis for RUD cannot be rejected for any of the 25 cm/pixel orthoimage sections, suggesting that most of the sections are consistent with a random ordering. RAM and RUD results for the 1 m/pixel orthoimage sections are similar to those for the 25 cm/pixel sections. In summary, thickness trends based on the 25 cm/pixel orthoimages are most consistent with random variations in bed thickness, although alternating frequently between high and low values, and suggest a lack of significant

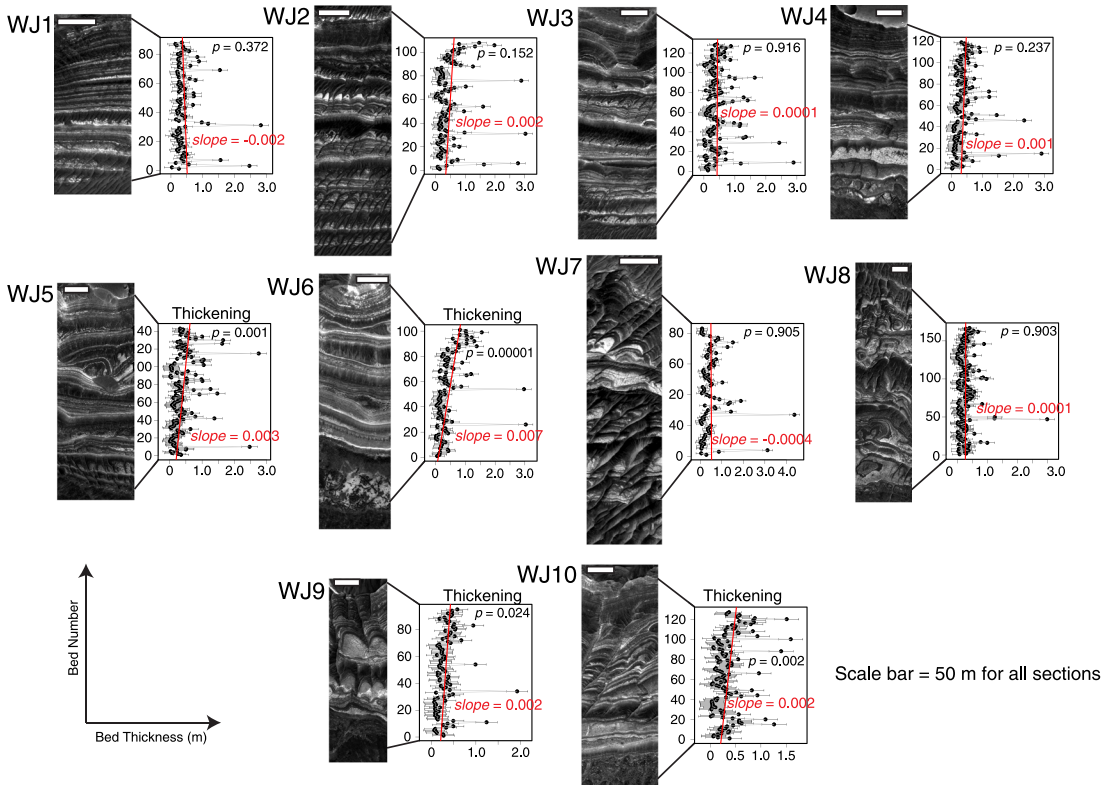

Figure 10. Bed thickness displayed as a function of stratigraphic position for sections measured on the plateau west of Juventae Chasma. Slope values (bed thickness/bed number) are displayed in red. For p less than 0.05, the null hypothesis is rejected and the section is assigned a thinning of thickening trend. Scale bar = 50 m.

thinning or thickening upward trends in the Holden sections. Runs testing of the 1 m/pixel thickness values is consistent with the 25 cm/pixel results, although the tests for thinning and thickening upward suggest several trends present in the 1 m/pixel data set that do not appear in the 25 cm/pixel data.

4.1.3. Bed Thickness Distributions

[39] The histogram and CF plots for the 25 cm/pixel and 1 m/pixel orthoimage results are qualitatively very similar, so only the 25 cm/pixel plots are discussed in detail.

[40] Histograms for Holden sections show that thickness frequency distributions are generally unimodal and positively skewed, although H5 is an exception (Figure 13). Sections H2–H9 exhibit modes less than 40 cm, and only sections H1 and H10 exhibit modes greater than or equal to 40 cm. Holden sections, excluding H1, H6, and H10, show an offset between the mode and the mean thickness, with the mode being less than the mean bed thickness.

[41] Holden CF plots show that bed thickness measurements are generally best described by lognormal CDFs (Figure 14). Theoretical exponential CDFs tend to overestimate the number of thin beds measured in the stratigraphic sequences and underestimate the frequency of thick beds. Sections H5-H8 offer good examples of this disparity. For H2 and H9, the theoretical lognormal and exponential CDFs offer comparable fits to bed thickness measurements. In general, the theoretical normal CDFs do not match well with the measured data, overestimating the number of thin beds and underestimating beds of intermediate thickness.

[42] The Lilliefors test of normality for both the 25 cm/pixel and 1 m/pixel data sets suggests that the normal distribution is a poor fit for the Holden sections. This result is consistent with CF plots in Figure 14. The null hypothesis is confidently rejected at a 95% significance level or higher for all 25 cm/pixel sections except H5. Lilliefors testing for lognormality reveals that the null hypothesis cannot be rejected at a 95% significance level for 8 of the 10 25 cm/pixel Holden sections. Meanwhile, the null hypothesis for exponentiality is rejected at a 95% significance level or higher for all Holden sections, suggesting that this distribution is a poor fit to the data. Statistical testing of the 1 m/pixel orthoimage bed thicknesses produces similar results to the 25 cm/pixel data, with most sections rejecting the null hypothesis for normal and exponential distributions but failing to reject lognormality for 9 of 10 sections. These results suggest that bed thickness measurements for Holden sections are most consistent with lognormal distributions.

4.1.4. Log-Log Plots

[43] Sections H3, H4, and H7 may come closest to a power-law trend based on visual inspection of the plots in Figure 15, but thicknesses measured in Holden sections generally do not follow power-law behavior over the full range of the data set. The thinnest and thickest beds in the sections consistently deviate from a linear trend in the log-log plots. In some cases, rollover of bed thickness frequency is identified by a sharp break in slope, as in sections H2 and H9. Interestingly, Lilliefors tests for H2 reject the normal, lognormal, and exponential distributions (Table 5), raising the possibility that this

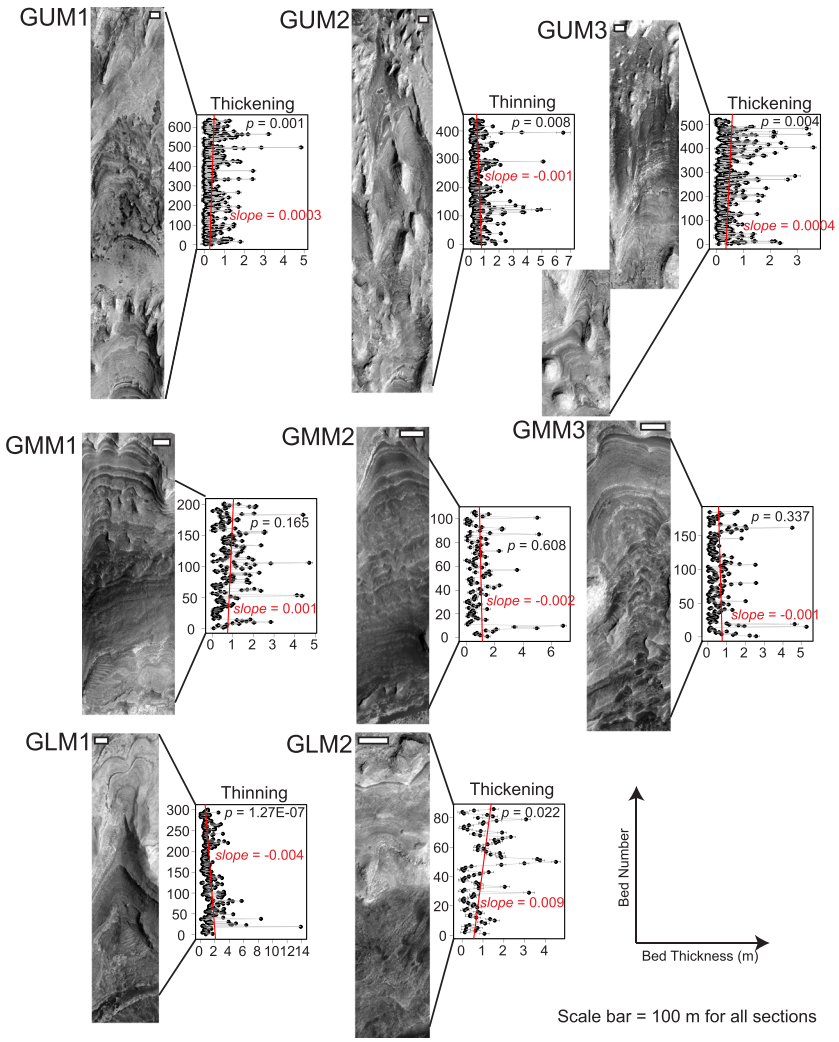

Figure 11. Bed thickness displayed as a function of stratigraphic position for sections measured in Gale Crater. Slope values (bed thickness/bed number) are displayed in red. For p less than 0.05, the null hypothesis is rejected and the section is assigned a thinning of thickening trend. Scale bar = 100 m.

section may be most consistent with a modified power law. For other sections, the dropoff in thin beds is more gradual (i.e., H1, H4, H5) and Lilliefors testing shows that bed thicknesses are consistent with lognormal distributions.

4.2. Plateau West of Juventae

4.2.1. Bed Thickness Statistics

[44] Sections measured on the plateau west of Juventae range between 30 and 70 m in total thickness (Table 3). The 1 m/pixel sections contain between 36 and 119 beds per section (Table 3), whereas 25 cm/pixel sections contain between one and two times as many beds, ranging from 83 beds in WJ7 to as many as 167 beds in WJ8. Mean bed thickness measured with 25 cm/pixel orthoimages ranges from ~30 cm (WJ8) to ~50 cm (WJ7), while mean bed thickness measured with 1 m/pixel orthoimages is between ~50 cm (WJ3, WJ8) to more than 1 m (WJ7). There are differences in the number of beds and mean bed thickness of the 25 cm/pixel and 1 m/pixel sections, but minimum and maximum bed thickness measured in the two data sets is similar. In fact, the maximum bed thickness measured with the 1 m/pixel orthoimages is sometimes smaller than the corresponding maximum thickness measured with the 25 cm/pixel orthoimage (i.e., WJ1-WJ3).

4.2.2. Trends in Thickness Versus Stratigraphic Position

[45] Six of ten sections on the plateau west of Juventae exhibit no statistically significant thinning or thickening upward trends when measured with the 25 cm/pixel orthoimage (Figure 10). Four sections show statistically significant thickening upward trends (WJ5, WJ6, WJ9, and WJ10). For sections where possible thickening trends have been identified, the estimated error bars are generally small enough that they do not span the full range of measured thicknesses. WJ9 and WJ10 may be exceptions. The 1 m/pixel results are similar to those obtained with the 25 cm/pixel data set (Table A2), with 6 of 10 sections showing no thickening or thinning upward trends but with sections WJ3, WJ5, WJ6, and WJ8 all exhibiting thickening upward trends.

[46] Significance testing for RAM reveals that 9 of 10 sections on the plateau west of Juventae measured with the 25 cm/pixel orthoimage are consistent with a nonrandom ordering of deviations above or below mean thickness, suggesting frequent alternations between high and low values

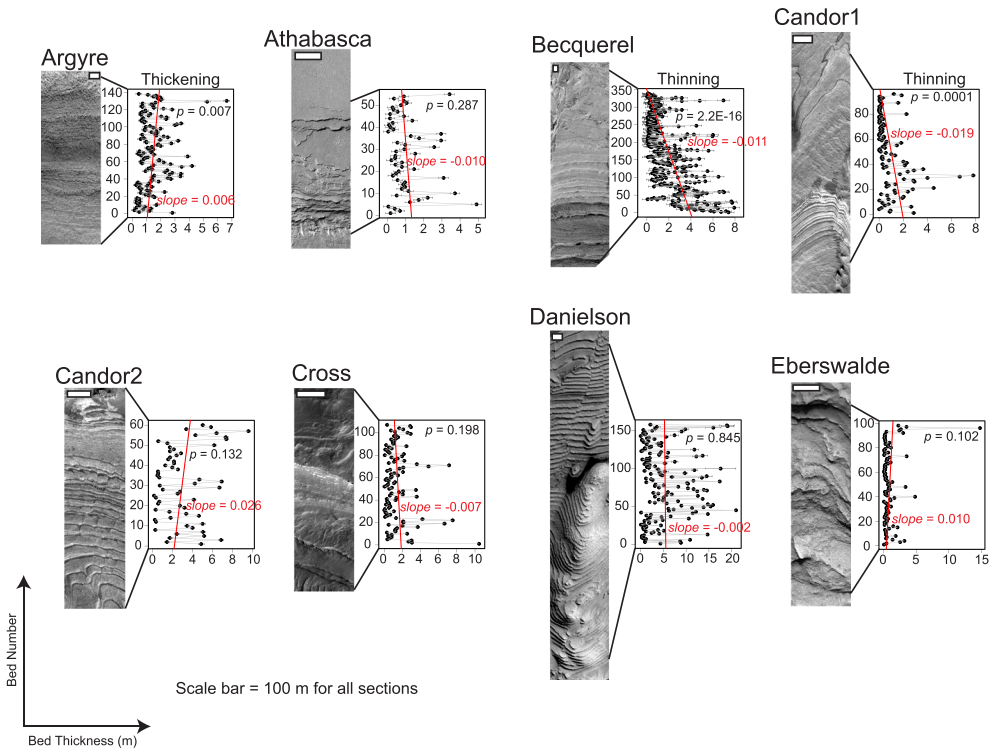

Figure 12. Bed thickness displayed as a function of stratigraphic position for sections measured in Argyre Planitia, Athabasca Valles, Becquerel Crater, Candor Crater, Cross Crater, Eberswalde Crater, and Danielson Crater. Slope values (bed thickness/bed number) are displayed in red. For p less than 0.05, the null hypothesis is rejected and the section is assigned a thinning of thickening trend. Scale bar = 100 m.

(Table 4). The 1 m/pixel orthoimage results are similar, with the RAM null hypothesis failing to be rejected for only 2 sections (Table 4). RUD testing shows that only 3 of west Juventae plateau sections are random in both the 25 cm/pixel and 1 m/pixel data sets, although of these 3 sections only WJ9 is common between the two data sets. These results indicate that sections on the plateau west of Juventae exhibit nonrandom bed thickness variations with stratigraphic position, with several sections thickening upwards.

4.2.3. Bed Thickness Distributions

[47] The histogram and CF plots for the 25 cm/pixel and 1 m/pixel orthoimage results are qualitatively very similar, so only the 25 cm/pixel plots are discussed in detail. Histograms reveal a high frequency of thin beds present in the west Juventae plateau sections (Figure 13). The mode commonly occurs at the thinnest bed interval (as in sections WJ2, WJ4, WJ5, and WJ6-WJ9), and histograms show an offset between the mean bed thickness and the mode, where modal bed thickness is thinner than mean thickness.

[48] Theoretical lognormal and exponential CDFs match well with the frequency of measured bed thickness (Figure 14). Exponential CDFs overestimate the number of thin beds present in several sections (WJ1, WJ9) and in some cases underestimate the frequency of intermediate thickness beds (WJ7-WJ9), but disparity in the quality of fits provided by lognormal and exponential CDFs is not obvious for these sections.

[49] In contrast, normal CDFs consistently overpredict the frequency of thin beds and underpredict the number of intermediate thickness beds. This is consistent with the Lilliefors tests of normality, which suggest that the normal distribution is a poor fit for all of the 25 cm/pixel and 1 m/pixel measured sections on the plateau west of Juventae (Table 5). Of the 10 sections measured here, the null hypothesis for lognormality is rejected at a 95% significance level or higher for half of the sections in both the 25 cm/pixel (WJ1, WJ3, WJ5, WJ8, WJ10) and 1 m/pixel (WJ3, WJ5, WJ7, WJ8, WJ10) orthoimages. The null hypothesis for exponentiality is rejected at a 95% significance level or higher for 7 of the sections measured with the 25 cm/pixel orthoimage, and for 8 of 10 sections measured with the 1 m/pixel orthoimage. All three distributions are rejected for sections WJ3, WJ8, and WJ10 in both the 25 and 1 m/pixel orthoimages, suggesting that a distribution other than those examined here may better explain these bed thickness measurements.

4.2.4. Log-Log Plots

[50] Sections on the west plateau of Juventae do not exhibit power-law behavior over the full range of measured bed thickness values (Figure 15). Sections exhibit a gradual deviation from power-law behavior for thin beds starting between 20 and 40 cm. The thickest beds measured in the sections also deviate from an expected power-law trend.

4.3. Gale Crater

4.3.1. Bed Thickness Statistics

[51] Total thickness for the sections measured in Gale crater ranges from ~84 m (GLM2, 25 cm orthoimage) to more than 400 m (GLM1) (Table 3). Using the 25 cm/pixel orthoimages, 300 and 86 beds were identified in sections

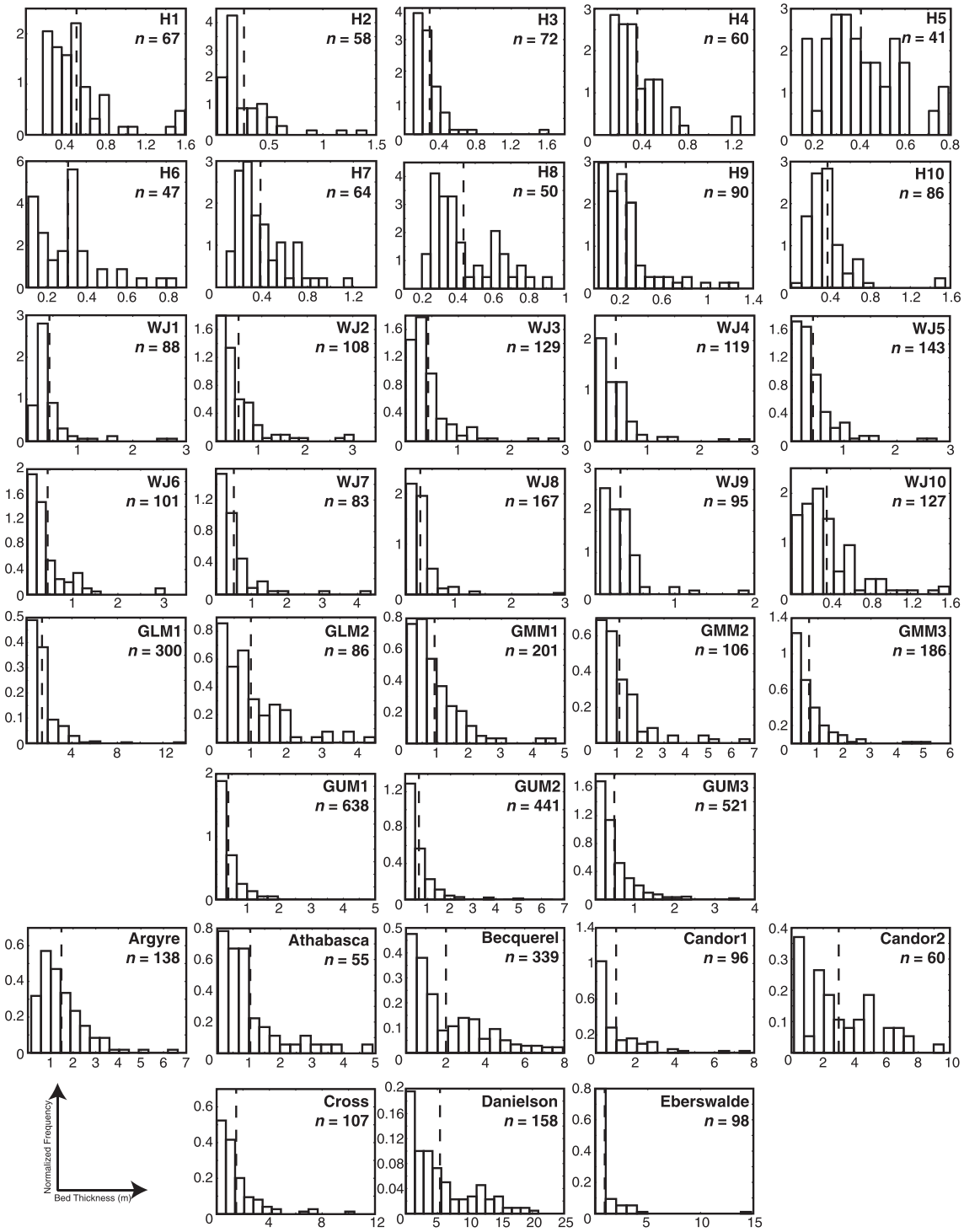

Figure 13. Histograms of sections in Holden, west Juventae plateau, Gale, Argyre, Athabasca, Becquerel, Candor Chasma, Cross, Eberswalde, and Danielson. Histograms are normalized so that the total area sums to 1. The dashed line indicates the mean thickness, and *n* is the number of beds measured for each section.

GLM1 and GLM2, respectively. Half as many beds were tabulated for GLM1 using the 1 m/pixel orthoimage, but section GLM2 maintained 69 beds. The middle member sections, GMM1, GMM2, and GMM3, contain between 106–201 beds in the 25 cm/pixel data set but only 52–94 beds when measured with the 1 m/pixel orthoimage. Mean bed thickness is greatest for GLM1 (1.29 m with 25 cm/pixel orthoimage, 2.57 m with 1 m/pixel) and decreases upsection, with middle member 25 cm/pixel mean thickness ranging from ~0.66 to 1 m. Upper member sections contain the smallest mean thickness between ~0.40 and 60 cm. Mean bed thickness decreases upsection using the lower resolution orthoimage as well, but with middle member mean thickness ranging from 1.61–1.96 m and upper member thickness ranging

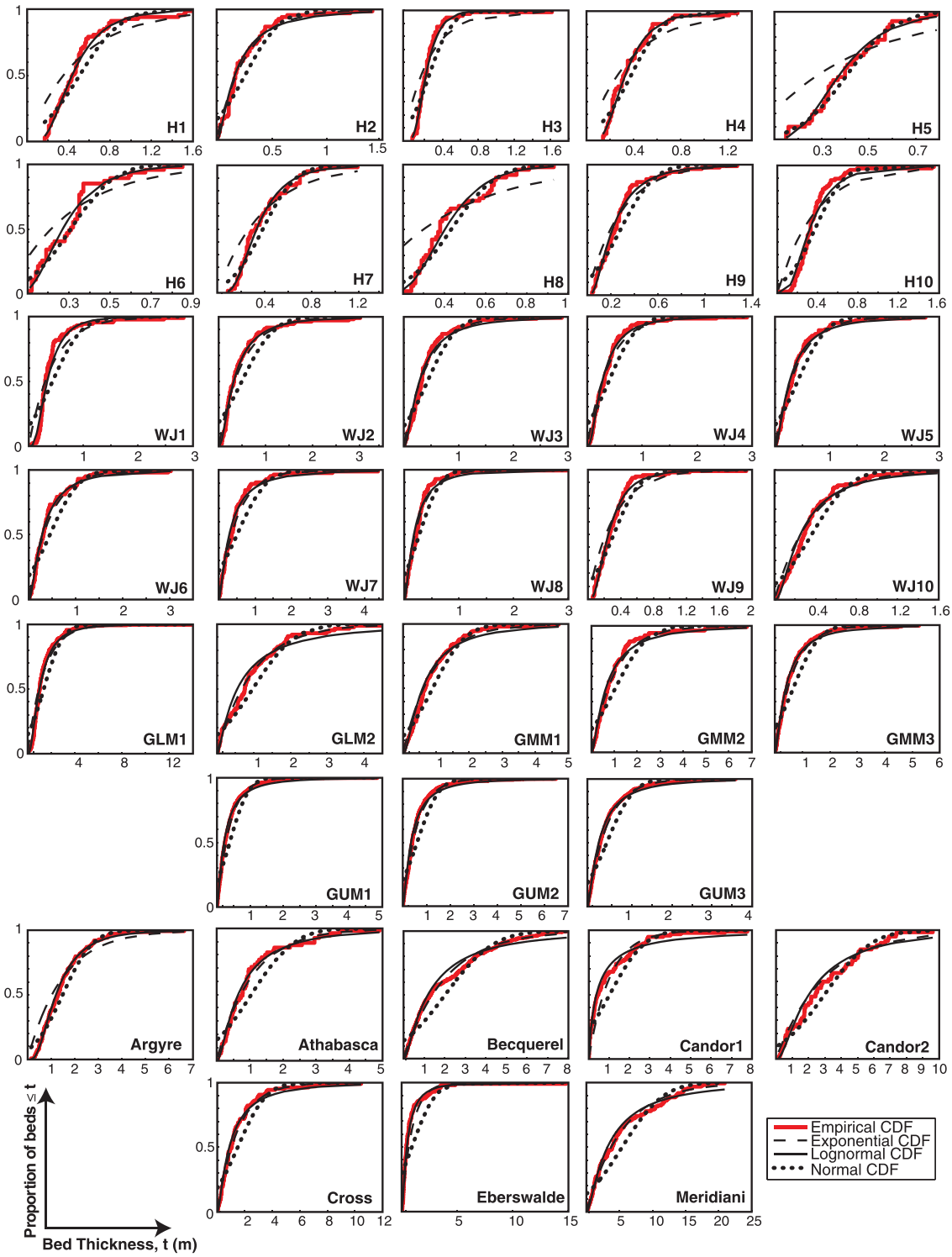

Figure 14. Plots of empirical CDFs and theoretical exponential, lognormal, and normal CDFs for bed thickness measured in Holden, west Juventae plateau, Gale, Argyre, Athabasca, Becquerel, Candor Chasma, Cross, Eberswalde, and Danielson.

from 0.86 cm to ~1 m. Minimum measured bed thickness for all sections, whether measured with the 25 cm/pixel orthoimage or the 1 m/pixel image, is <10 cm. However, maximum bed thickness varies between the sections, with the thickest beds in the lower member sections.

4.3.2. Trends in Thickness Versus Stratigraphic Position

[52] Five of eight Gale sections show statistically significant thinning or thickening upward trends when measured with 25 cm/pixel orthoimages (Figure 11). GLM1 and GUM2 show thinning upward trends, while GLM2,

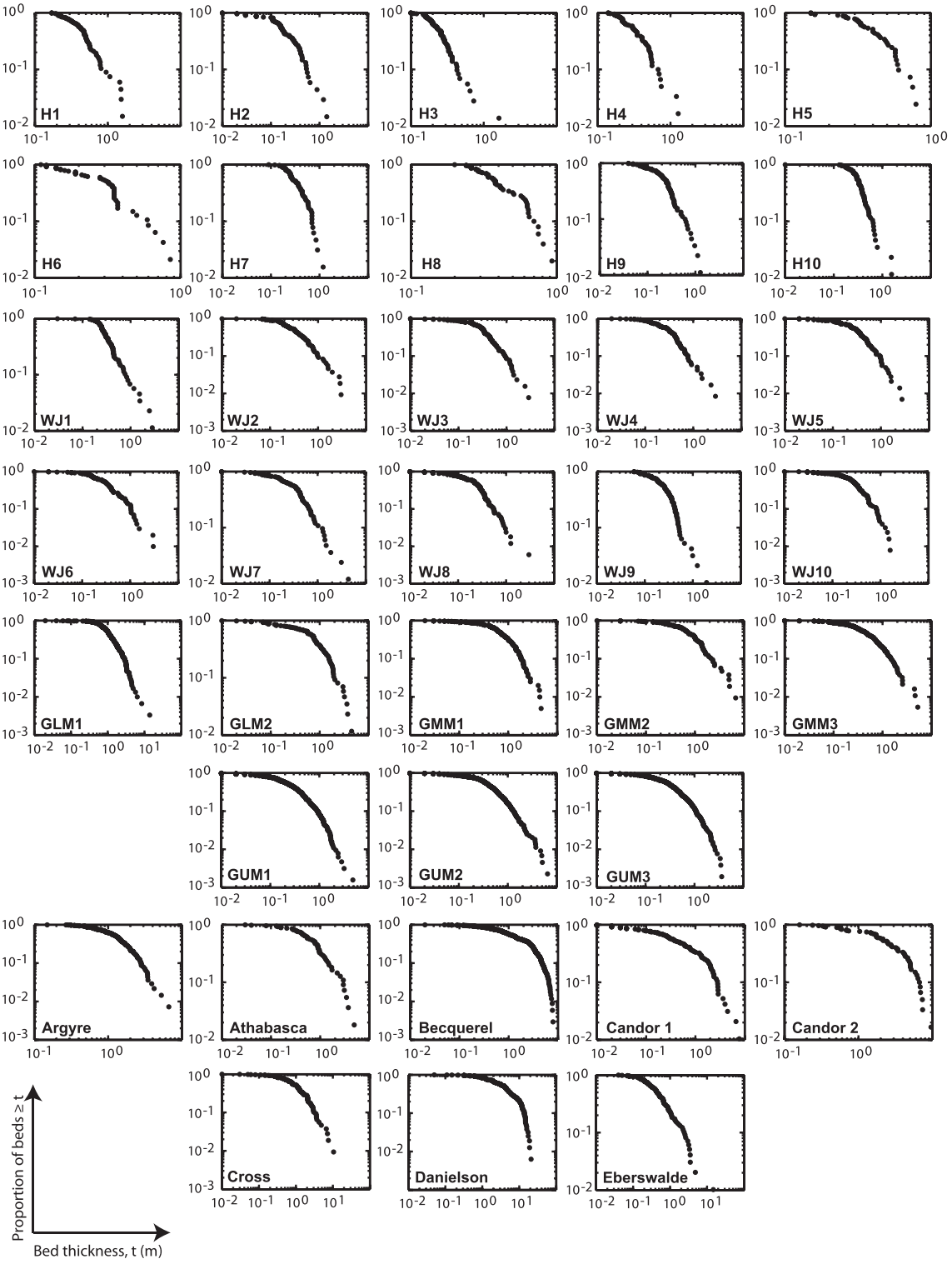

Figure 15. Log-log plots displaying the proportion of bed thickness values greater than or equal to *t* for sections measured in Holden, west Juventae plateau, Gale, Argyre, Athabasca, Becquerel, Candor Chasma, Cross, Eberswalde, and Danielson.

GUM1, and GUM3 show thickening trends. Using data extracted with the 1 m/pixel orthoimage (Table A2), four of eight Gale sections show thinning or thickening upward trends, with GLM2 and GUM2 thinning upward and GMM1 and GUM3 thickening upward.

[53] Significance testing for RAM reveals that the null hypothesis of randomness is rejected for all eight Gale sections measured with the 25 cm/pixel orthoimage and for all but GMM2 measured with the 1 m/pixel orthoimages (Table 4). Meanwhile, the RUD null hypothesis is rejected

Table 3. Basic Bed Thickness Statistics

		25 cm/pixel						1 m/pixel					
Location	Outcrop Slope	Total Section Thickness (m)	n	μ(m)	σ(m)	Min t (m)	Max t (m)	Total Section Thickness (m)	n	μ(m)	σ(m)	Min t (m)	Max t (m)
H1	0.19	34.0 ± 1.1	67	0.51 ± 0.02	0.32	0.17 ± 0.13	1.59 ± 0.13	34.9 ± 0.8	38	0.92 ± 0.02	0.79	0.19 ± 0.13	4.51 ± 0.13
H2	0.11	17.7 ± 2.8	68	0.26 ± 0.04	0.26	<0.10 ± 0.34	1.41 ± 0.34	16.0 ± 2.3	45	0.36 ± 0.05	0.30	<0.10 ± 0.34	1.63 ± 0.34
H3	0.15	20.3 ± 2.9	72	0.28 ± 0.02	0.20	0.10 ± 0.34	1.62 ± 0.34	23.3 ± 2.0	35	0.67 ± 0.06	0.48	0.20 ± 0.34	2.30 ± 0.34
H4	0.22	22.6 ± 2.7	60	0.38 ± 0.04	0.23	0.14 ± 0.35	1.28 ± 0.34	20.3 ± 1.8	28	0.73 ± 0.06	0.25	0.38 ± 0.34	1.35 ± 0.34
H5	0.34	16.7 ± 2.2	41	0.41 ± 0.05	0.16	0.15 ± 0.34	0.79 ± 0.34	19.7 ± 1.6	23	0.86 ± 0.07	0.28	0.51 ± 0.34	1.59 ± 0.34
H6	0.24	14.5 ± 2.3	47	0.31 ± 0.05	0.17	0.11 ± 0.34	0.85 ± 0.34	15.8 ± 1.8	28	0.56 ± 0.06	0.33	0.13 ± 0.34	1.39 ± 0.34
H7	0.25	24.8 ± 2.7	64	0.39 ± 0.04	0.22	<0.10 ± 0.34	1.19 ± 0.34	25.0 ± 2.1	39	0.64 ± 0.06	0.36	0.10 ± 0.34	1.83 ± 0.34
H8	0.28	21.7 ± 2.4	50	0.43 ± 0.05	0.17	0.2 ± 0.34	0.93 ± 0.34	25.5 ± 1.9	32	0.80 ± 0.06	0.58	0.34 ± 0.34	3.57 ± 0.34
H9	0.13	25.2 ± 3.2	90	0.28 ± 0.04	0.23	<0.10 ± 0.34	1.27 ± 0.34	25.3 ± 2.4	49	0.52 ± 0.05	0.36	<0.10 ± 0.34	1.45 ± 0.34
H10	0.16	32 ± 1.2	86	0.37 ± 0.01	0.23	<0.10 ± 0.13	1.55 ± 0.13	32.8 ± 0.9	48	0.68 ± 0.05	0.41	0.24 ± 0.13	2.88 ± 0.13
WJ1	0.20	38.3 ± 2.3	88	0.44 ± 0.03	0.43	<0.10 ± 0.24	2.83 ± 0.24	44.4 ± 2.0	67	0.66 ± 0.03	0.47	<0.10 ± 0.24	2.77 ± 0.24
WJ2	0.15	53.0 ± 2.5	108	0.49 ± 0.02	0.55	<0.10 ± 0.24	3.02 ± 0.24	53.5 ± 2.2	83	0.64 ± 0.03	0.51	<0.10 ± 0.24	2.92 ± 0.24
WJ3	0.16	55.7 ± 2.7	129	0.43 ± 0.02	0.43	<0.10 ± 0.24	2.89 ± 0.24	58.1 ± 2.6	119	0.49 ± 0.02	0.41	<0.10 ± 0.24	2.60 ± 0.24
WJ4	0.15	46.9 ± 2.6	119	0.39 ± 0.02	0.41	<0.10 ± 0.24	2.91 ± 0.24	47.4 ± 2.2	85	0.56 ± 0.02	0.50	<0.10 ± 0.24	3.03 ± 0.24
WJ5	0.16	58.9 ± 2.9	143	0.41 ± 0.02	0.42	<0.10 ± 0.24	2.75 ± 0.24	70.1 ± 2.5	108	0.65 ± 0.02	0.66	<0.10 ± 0.24	4.15 ± 0.24
WJ6	0.13	45.7 ± 2.4	101	0.45 ± 0.02	0.50	<0.10 ± 0.24	3.03 ± 0.24	48.4 ± 1.8	58	0.83 ± 0.03	0.77	<0.10 ± 0.24	3.41 ± 0.24
WJ7	0.12	42.0 ± 2.2	83	0.51 ± 0.03	0.64	<0.10 ± 0.24	4.37 ± 0.24	42.9 ± 1.4	36	1.19 ± 0.04	1.20	<0.10 ± 0.24	5.49 ± 0.24
WJ8	0.06	46.5 ± 3.1	167	0.28 ± 0.02	0.31	<0.10 ± 0.24	2.99 ± 0.24	45.3 ± 2.3	89	0.51 ± 0.03	0.49	<0.10 ± 0.24	3.82 ± 0.24
WJ9	0.19	30.0 ± 2.3	95	0.32 ± 0.02	0.26	<0.10 ± 0.24	1.93 ± 0.24	31.6 ± 1.6	43	0.73 ± 0.04	0.63	0.15 ± 0.24	3.60 ± 0.24
WJ10	0.10	45.8 ± 2.7	127	0.36 ± 0.02	0.30	<0.10 ± 0.24	1.59 ± 0.24	48.0 ± 1.9	62	0.77 ± 0.03	0.63	<0.10 ± 0.24	2.90 ± 0.24
GLM1	0.20	410.4 ± 2.3	300	1.37 ± 0.01	1.29	<0.10 ± 0.13	13.9 ± 0.20	403.4 ± 1.7	157	2.57 ± 0.01	2.36	<0.10 ± 0.13	16.08 ± 0.15
GLM2	0.22	83.8 ± 2.1	86	0.97 ± 0.02	0.92	<0.10 ± 0.22	4.49 ± 0.22	129.9 ± 1.8	69	1.88 ± 0.03	2.94	<0.10 ± 0.22	19.05 ± 0.26
GMM1	0.18	179.0 ± 1.9	201	0.89 ± 0.01	0.79	<0.10 ± 0.14	4.71 ± 0.16	179.1 ± 1.3	94	1.91 ± 0.01	1.58	<0.10 ± 0.13	7.72 ± 0.14
GMM2	0.17	108.8 ± 2.2	106	1.03 ± 0.02	1.12	<0.10 ± 0.22	6.79 ± 0.21	101.9 ± 1.6	52	1.96 ± 0.03	2.54	<0.10 ± 0.22	15.55 ± 0.23
GMM3	0.19	123.5 ± 1.6	186	0.66 ± 0.01	0.76	<0.10 ± 0.13	5.25 ± 0.13	128.9 ± 1.1	80	1.61 ± 0.01	1.66	<0.10 ± 0.12	8.92 ± 0.15
GUM1	0.11	247.2 ± 3.4	638	0.39 ± 0.01	0.45	<0.10 ± 0.21	4.85 ± 0.13	237.1 ± 3.9	275	0.86 ± 0.01	0.92	<0.10 ± 0.44	7.44 ± 0.14
GUM2	0.14	268.4 ± 2.9	441	0.61 ± 0.01	0.73	<0.10 ± 0.12	6.49 ± 0.49	258.1 ± 2.9	275	0.94 ± 0.01	1.10	<0.10 ± 0.48	6.8 ± 0.57
GUM3	0.13	246.0 ± 2.5	521	0.47 ± 0.00	0.52	<0.10 ± 0.11	3.6 ± 0.11	239.4 ± 1.7	232	1.03 ± 0.01	0.97	<0.10 ± 0.12	5.04 ± 0.12
Argyre	0.23	204.8 ± 2.4	138	1.48 ± 0.02	1.01	0.15 ± 0.20	6.63 ± 0.21	207.3 ± 1.7	69	3.00 ± 0.03	1.69	0.16 ± 0.21	9.09 ± 0.24
Athabasca	0.06	57.6 ± 2.0	55	1.05 ± 0.04	1.04	<0.10 ± 0.27	4.91 ± 0.27	46.2 ± 1.5	32	1.45 ± 0.05	1.48	<0.10 ± 0.27	7.05 ± 0.27
Becquerel	0.11	685.9 ± 9.2	339	2.02 ± 0.03	1.86	<0.10 ± 0.5	7.93 ± 0.5	702.2 ± 8.0	261	2.69 ± 0.03	2.08	<0.10 ± 0.50	12.13 ± 0.52
Candor1	0.04	98.6 ± 1.7	96	1.03 ± 0.02	1.37	<0.10 ± 0.18	7.78 ± 0.17	110.1 ± 1.4	61	1.80 ± 0.02	1.68	<0.10 ± 0.18	7.16 ± 0.21
Candor2	0.13	178.8 ± 1.5	60	2.98 ± 0.03	2.27	0.16 ± 0.17	9.61 ± 0.20	182.9 ± 1.4	48	3.81 ± 0.03	2.48	<0.10 ± 0.17	8.18 ± 0.25
Cross	0.28	159.0 ± 2.0	107	1.49 ± 0.02	1.65	<0.10 ± 0.19	10.45 ± 0.19	152.2 ± 1.1	31	4.91 ± 0.03	5.37	0.78 ± 0.19	23.99 ± 0.20
Danielson	0.04	855.0 ± 6.6	158	5.41 ± 0.04	4.98	<0.10 ± 0.33	20.93 ± 0.26	964.3 ± 2.8	99	9.74 ± 0.03	10.05	0.14 ± 0.26	82.04 ± 0.80
Eberswalde	0.12	90.6 ± 1.6	98	0.92 ± 0.02	1.69	<0.10 ± 0.16	14.8 ± 0.16	86.2 ± 1.2	57	1.51 ± 0.02	2.21	0.12 ± 0.16	15.44 ± 0.16

Table 4. Runs Test Significance Probability Values

	25 cm/pixel						1 m/pixel					
	RAM			RUD			RAM			RUD		
Location	*p* Value	Reject H_0?	No. of Runs	*p* Value	Reject H_0?	No. of Runs	*p* Value	Reject H_0?	No. of Runs	*p* Value	Reject H_0?	No. of Runs
H1	0.001	Yes	18	0.402	No	47	0.001	Yes	8	0.257	No	21
H2	0.000	Yes	12	0.382	No	37	0.006	Yes	14	0.045	Yes	23
H3	0.000	Yes	14	0.156	No	39	0.499	No	15	0.630	No	24
H4	0.000	Yes	15	0.796	No	41	0.014	Yes	8	0.049	Yes	13
H5	0.585	No	19	0.218	No	22	1.000	No	12	0.791	No	14
H6	0.007	Yes	15	0.860	No	30	0.017	Yes	8	0.394	No	16
H7	0.008	Yes	21	0.726	No	44	0.004	Yes	11	0.199	No	20
H8	0.000	Yes	12	0.600	No	33	0.050	Yes	10	0.214	No	17
H9	0.000	Yes	24	0.831	No	57	0.010	Yes	16	0.186	No	28
H10	0.788	No	39	0.177	No	50	0.010	Yes	15	0.448	No	29
WJ1	0.138	No	29	0.327	No	54	1.000	No	31	0.034	Yes	36
WJ2	0.000	Yes	20	0.563	No	68	0.012	Yes	29	0.023	Yes	44
WJ3	0.000	Yes	35	0.000	Yes	67	0.000	Yes	37	0.008	Yes	64
WJ4	0.002	Yes	41	0.002	Yes	62	0.000	Yes	22	0.276	No	51
WJ5	0.000	Yes	39	0.002	Yes	75	0.000	Yes	25	0.000	Yes	52
WJ6	0.000	Yes	16	0.010	Yes	52	0.000	Yes	12	0.225	No	34
WJ7	0.002	Yes	23	0.001	Yes	41	0.061	No	11	0.004	Yes	16
WJ8	0.000	Yes	56	0.002	Yes	89	0.010	Yes	32	0.024	Yes	49
WJ9	0.000	Yes	24	0.424	No	56	0.030	Yes	14	0.295	No	25
WJ10	0.000	Yes	35	0.033	Yes	70	0.040	Yes	21	0.035	Yes	33
GLM1	0.000	Yes	85	0.016	Yes	181	0.000	Yes	52	0.080	No	94
GLM2	0.000	Yes	25	0.000	Yes	40	0.001	Yes	20	0.003	Yes	35
GMM1	0.000	Yes	57	0.152	No	124	0.001	Yes	30	0.150	No	56
GMM2	0.018	Yes	36	0.373	No	66	0.494	No	19	0.778	No	35
GMM3	0.000	Yes	49	0.837	No	120	0.008	Yes	24	1.000	No	53
GUM1	0.000	Yes	169	0.517	No	411	0.000	Yes	77	0.007	Yes	161
GUM2	0.000	Yes	122	0.000	Yes	255	0.000	Yes	87	0.007	Yes	161
GUM3	0.000	Yes	139	0.215	No	330	0.000	Yes	71	0.111	No	143
Argyre	0.004	Yes	50	0.660	No	89	0.016	Yes	25	0.360	No	42
Athabasca	0.201	No	20	0.9568	No	37	0.0771	No	10	0.5149	No	19
Becquerel	0.000	Yes	56	0.0077	Yes	202	1.26E-16	Yes	64	0.0015	Yes	151
Candor1	0.008	Yes	31	0.1766	No	57	0.0613	No	23	0.329	No	44
Candor2	0.088	No	23	0.7956	No	41	0.3262	No	21	0.949	No	31
Cross	0.003	Yes	34	0.2614	No	65	0.2403	No	9	0.9479	No	21
Danielson	0.021	Yes	59	0.9244	No	106	0.3918	No	54	0.968	No	66
Eberswalde	0.008	Yes	26	0.6558	No	62	0.792	No	22	0.9576	No	38

for only the two GLM sections and GUM2 using the 25 cm/pixel orthoimages. The remaining sections are consistent with a random distribution of thicknesses. Using the 1 m/pixel orthoimage data and the RUD test, randomness is rejected for GLM2, GUM1, and GUM2. These results indicate that observed bed thickness variations may be nonuniform in Gale, even within a given member of the Lower formation. RAM tests show that bed thickness variations are nonrandom (Table 4), but some sections in a given member are consistent with thinning upward trends while other sections in that member are consistent with thickening upward trends.

4.3.3. Bed Thickness Distributions

[54] Gale histograms show that bed thickness is positively skewed and beds most frequently fall into the thinnest histogram bins (Figure 13). Mean thickness is offset from modal thickness for all sections, with the mode being less than the mean thickness.

[55] Both lognormal and exponential CDFs match reasonably well with the bed thickness measurements obtained from lower Mt. Sharp (Figure 14). Normal CDFs provide a poor match to the measured data, overpredicting the frequency of thin beds and underpredicting intermediate beds. Results of Lilliefors testing (Table 5) are generally consistent with the histograms and CF plots. The normal distribution is rejected for all eight Gale sections using both the 25 cm/pixel and 1 m/pixel orthoimages. Seven of eight Gale sections measured with the 25 cm/pixel orthoimage and five of the eight sections measured with the 1 m/pixel orthoimage reject the lognormal null hypothesis. Exponentiality is rejected for only three of the eight Gale sections measured with the 25 cm/pixel orthoimage (GLM1, GMM1, GUM2) and for only GLM1 and GUM3 1 m/pixel orthoimage sections. These results suggest that exponential distributions, rather than lognormal distributions, provide the best fit to the data.

4.3.4. Log-Log Plots

[56] Gale thickness distributions do not show power-law behavior (Figure 15). Data sets experience gradual deviation of thin beds from the expected power-law trend. The thickest beds also deviate from power-law behavior (i.e., GMM1, GMM2, GMM3).

4.4. Additional Sections

4.4.1. Bed Thickness Statistics

[57] Total section thickness at the other locations examined in this study ranges from ~50 m (Athabasca) to nearly 1 km (Danielson) (Table 3). The Becquerel and Danielson sections

Table 5. Lilliefors Probability Significance Values

	p Values (Lilliefors)					
	25 cm/pixel			1 m/pixel		
Location	Normal	Lognormal	Exponential	Normal	Lognormal	Exponential
H1	<0.001	0.276	<0.001	<0.001	>0.500	0.004
H2	<0.001	<0.001	0.010	0.005	0.003	0.083
H3	<0.001	0.212	<0.001	<0.001	0.275	<0.001
H4	<0.001	0.065	<0.001	0.006	0.084	<0.001
H5	0.342	>0.500	<0.001	0.021	0.296	<0.001
H6	<0.001	0.059	<0.001	0.008	>0.500	<0.001
H7	<0.001	0.115	<0.001	0.371	0.229	<0.001
H8	<0.001	0.056	<0.001	<0.001	>0.500	<0.001
H9	<0.001	0.240	0.002	0.020	0.139	0.068
H10	<0.001	0.015	<0.001	0.001	0.357	<0.001
WJ1	<0.001	0.001	<0.001	<0.001	0.079	<0.001
WJ2	<0.001	0.086	0.003	<0.001	>0.500	<0.001
WJ3	<0.001	<0.001	0.001	<0.001	<0.001	0.004
WJ4	<0.001	0.136	0.004	<0.001	0.122	0.025
WJ5	<0.001	<0.001	0.052	<0.001	0.014	0.008
WJ6	<0.001	0.244	0.070	<0.001	0.438	>0.500
WJ7	<0.001	0.056	0.251	<0.001	0.003	0.180
WJ8	<0.001	<0.001	0.019	<0.001	<0.001	0.002
WJ9	<0.001	0.378	0.001	0.001	>0.500	0.015
WJ10	<0.001	<0.001	0.002	<0.001	0.005	<0.001
GLM1	<0.001	<0.001	<0.001	<0.001	0.086	<0.001
GLM2	<0.001	<0.001	0.261	<0.001	0.075	0.100
GMM1	<0.001	<0.001	<0.001	0.001	0.012	0.281
GMM2	<0.001	0.008	0.324	<0.001	0.405	0.063
GMM3	<0.001	0.078	0.401	<0.001	0.019	0.394
GUM1	<0.001	<0.001	0.062	0.001	<0.001	0.179
GUM2	<0.001	<0.001	0.008	<0.001	<0.001	0.084
GUM3	<0.001	<0.001	0.054	<0.001	0.008	0.024
Argyre	<0.001	>0.500	<0.001	0.065	0.048	<0.001
Athabasca	<0.001	>0.500	>0.500	<0.001	0.276	>0.500
Becquerel	<0.001	<0.001	0.017	<0.001	<0.001	<0.001
Candor1	<0.001	0.159	<0.001	0.003	0.006	>0.500
Candor2	<0.001	0.046	0.128	0.002	0.034	0.008
Cross	<0.001	0.262	>0.500	<0.001	0.111	0.047
Danielson	<0.001	0.012	0.429	<0.001	0.001	0.074
Eberswalde	<0.001	>0.500	<0.001	<0.001	0.015	0.027

contain the most beds, 339 and 158, respectively, when measured with the 25 cm/pixel orthoimage. These same sections contain only 261 and 99 beds when measured with the 1 m/pixel orthoimage. Mean bed thickness for the additional sections ranges between ~1 and 3 m, although Danielson is an exception with a mean bed thickness of 5.41 m. Mean bed thickness increases significantly for several of the sections when using the 1 m/pixel orthoimage. For example, mean bed thickness in Cross crater is 1.49 m using the 25 cm/pixel orthoimage but increases to nearly 5 m with the 1 m/pixel orthoimage. Mean bed thickness also increases in Danielson from ~5 to nearly 10 m.

4.4.2. Trends in Thickness Versus Stratigraphic Position

[58] According to bed thickness measurements made with the 25 cm/pixel orthoimage, only Argyre, Becquerel, and Candor1 show statistically significant thinning or thickening trends, with Argyre thickening upward and Becquerel and Candor1 thinning upward (Figure 12). When using bed thickness measurements extracted from the 1 m/pixel orthoimages, only Eberswalde shows a significant trend, thickening upward (Table A2).

[59] The RAM significance testing of the 25 cm/pixel orthoimage sections reveals that all sections except Athabasca and Candor2 reject the null hypothesis of randomness about the mean (Table 4). In contrast, all but two 1 m/pixel sections fail to reject the RAM null hypothesis. Testing for RUD shows that all sections, both 25 cm/pixel and 1 m/pixel, fail to reject the null hypothesis except Becquerel. The RAM results are somewhat contradictory between the two data sets, making interpretation difficult, but it is clear that all sections but Becquerel are indistinguishable from a random distribution according to RUD testing.

4.4.3. Bed Thickness Distributions

[60] Histograms for these sections show that the most frequent bed thickness generally falls within the smallest bin (Figure 13). Argyre is the exception to this, but the distribution is still unimodal and positively skewed. As with other sections examined in this study, the mean is generally thicker than the mode.

[61] Cumulative frequency plots show that theoretical normal distributions do not provide a good fit to the data (Figure 14). Except for Argyre, the normal distribution overestimate the number of thin beds and underestimate the number of intermediate beds. Both exponential and lognormal distributions provide decent qualitative fits for the Athabasca, Becquerel, Candor, Cross, Danielson, Eberswalde sections. The Argyre section appears to be better described by the exponential fit, as the lognormal distribution overestimates the number of thin beds and underestimates the number of thick beds.

[62] Statistical testing helps support these qualitative observations (Table 5). Normal distributions are not a good fit because almost all sections measured, regardless of which orthoimage was used, reject the null hypothesis of normality at a significance level of 95% or higher. Lognormal distributions provide relatively good fits to the data, with only Becquerel, Candor2, and Danielson rejecting the lognormal null hypothesis. The results are nearly opposite when using the 1 m/pixel data, with all sections rejecting the null hypothesis of lognormality except Athabasca and Cross. Tests for exponentiality show that Athabasca, Candor2, Cross, and Danielson 25 cm/pixel sections fail to reject the null hypothesis, while others clearly reject the null hypothesis (Argyre, Becquerel, Candor1, and Eberswalde). Most noteworthy in these results is Becquerel, which is not consistent with any of the three distributions regardless of which orthoimage is used for analysis and for which it has been suggested that bed thicknesses are rhythmic and normally distributed [*Lewis et al*., 2008].

4.4.4. Log-Log Plots

[63] Log-log plots show that none of these additional sections follow power-law behavior over the full range of bed thickness values (Figure 15). Gentle rollover in the number of thin beds occurs between ~0.5 and 1 m for these sections, and thick beds also deviate from the expected linear trend.

5. Discussion

5.1. Bed Thickness on Mars

[64] The simplest possible interpretation of bed thickness on Mars is that thickness represents a sediment volume, and each bed records information about transport and dispersal during deposition. Thicker beds may signal larger sediment volumes and/or shorter dispersal length scales, whereas thin beds signal smaller sediment volumes and/or longer dispersal length scales. Therefore, bed thickness characteristics might help broadly bound the processes associated with accumulation of strata (transport, deposition, erosion) while providing additional criteria — similar to mineralogy, tone, or weathering pattern — for correlation of spatially distinct strata. Comparisons between the bed thickness properties of spatially distinct locations may reveal when deposits have experienced similar or different depositional histories. This study presents some of the ways that bed thickness can be used to learn more about the history and formation of sedimentary deposits on Mars, as well as some of the caveats associated with such an analysis.

5.2. Stratigraphic and Statistical Trends in Bed Thickness

5.2.1. Thinning and Thickening Trends

[65] In sedimentary basins on Earth, the deposition and accumulation of material are regulated by three main factors: sediment supply, base level, and rate of subsidence. In aqueous environments on Earth, the main role of tectonic subsidence in sediment deposition is in creating accommodation space and modulating base level. In the absence of tectonic controls, it is unclear what role, if any, subsidence would play in controlling the deposition, accumulation, and erosion of sedimentary materials on Mars over long timescales. Therefore, it is assumed that subsidence is not a primary control on the formation of most Martian sedimentary deposits [*Grotzinger and Milliken*, 2012]. In the absence of tectonically controlled subsidence, accommodation space is likely to be modulated more directly by sediment supply. Thus, even in the absence of subsidence, accommodation, sediment supply, and bed thickness likely vary — very generally — from proximal to distal along a single chronostratigraphic interval for certain depositional environments. For example, a simple alluvial fan system shows how these parameters vary systematically as a function of distance from the source (Figure 16). At the apex of the fan, fast-moving flows deposit thick, coarse-grained beds. Decrease in flow competence downdip results in an effective decrease in accommodation, and lower flow velocities lead to the deposition of thinner, finer-grained deposits.

[66] At odds with this simple model for alluvial fan bed thickness, the Holden sections show no systematic or statistically significant change in mean or maximum bed thickness, either increasing or decreasing, from H1 (located in a proximal setting closest to the expected sediment source) to H10 (a more distal location, farthest from the crater wall). This suggests that sediment supply, accommodation, and erosion rates were fairly constant over the area covered by these sections. Mean and maximum bed thicknesses also remain fairly constant over the area covered by WJ1-WJ10 on the plateau west of Juventae. The simplest interpretation of these observations is that the deposits in Holden crater and on the plateau west of Juventae Chasma represent fallout deposits — lacustrine, volcanic ash, or dust — where the depositional mechanisms predict greater lateral continuity of bed thickness. This hypothesis would be consistent with the deposits in Holden crater being lacustrine, as was suggested by *Grant et al*., [2008]. In addition, no clear trends in mean bed thickness are observed laterally between sections measured within the members of lower Mt. Sharp, suggesting that depositional conditions were also fairly consistent over this area of Gale crater at the member scale.

[67] Lateral changes in bed thickness reveal depositional and erosional conditions at a single time interval, but vertical thickening or thinning trends within a section express changes in depositional and erosional over time [*Fischer*, 1964; *Read and Goldhammer*, 1988]. Thick beds form when there is ample space for material to be deposited (increased accommodation); thin beds represent decreased accommodation [*Read and Goldhammer*, 1988]. After considering the results of significance testing and error analysis, it is clear that the 25 cm/pixel Holden sections show no significant increase or decrease in thickness vertically through the sections. The paucity of thinning or thickening trends in Holden may imply that sediment dispersal was uniform over time, occurring in an environment where suspended materials were advected over broad regions and settled out of suspension to form sheet deposits. This type of deposition might occur in subaqueous lacustrine (mud) or aeolian (dust, ash) settings where suspended fines settle out during quiescent periods. The lack of thinning or thickening trends in this location suggests that changes in base level may not have significantly influenced the formation of bedding, perhaps due to a constant sediment supply and lack of tectonic subsidence.

[68] On the plateau west of Juventae, 4 of the 10 25 cm/pixel sections exhibit a thickening upward trend at a statistically significant level, indicating that this trend may be real. However,

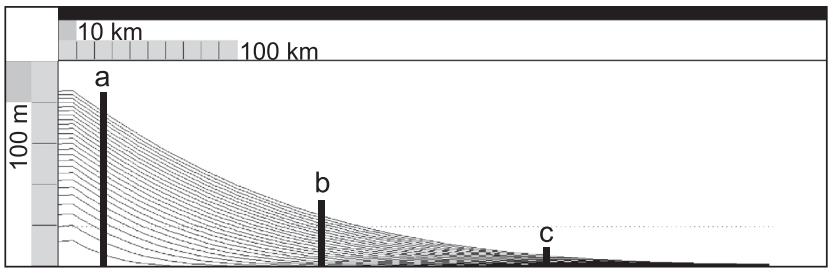

Figure 16. Stratigraphy of a simple alluvial fan modeled with STRATA [*Flemings and Grotzinger*, 1996], assuming constant flux of sediment and equal marine and non-marine diffusion constants. VE = 250. Note change in thickness of time-equivalent depositional sequences from the proximal location (a) to the median location (b) to the distal section (c).

because it is unclear why the other 6 sections at this location show no trend at all, it is difficult to speculate on the meaning of this trend. Consistent thickening or thinning trends are also not observed within the lower and upper member sections of Gale crater (Figure 11). Despite being within the same member, GLM1 shows an overall thinning trend, while GLM2 shows a thickening trend. Similarly, GUM1 and GUM3 show thickening trends, while GUM2 shows a thinning trend. As these sections are separated by several kilometers, it is possible that these disparate trends record distinct depositional conditions within the crater, but an alternative explanation is that these trends are due to variations in lighting, slope, or quality of exposed outcrop that induce apparent thinning and thickening. Trends within members at Gale crater are difficult to interpret and may be susceptible to image artifacts, but a systematic decrease in mean bed thickness upsection is observed in Gale crater over the Lower formation as a whole (Table 3). Mean bed thickness decreases from the lower to middle members, with the upper member sections exhibiting the thinnest means. The overall change in mean bed thickness between the members may suggest changes in sediment deposition and erosion rates through time on the member scale, rather than at the scale of individual beds. Therefore, the results presented here suggest that the morphological member boundaries and compositional changes identified by *Milliken et al.* [2010] may have been accompanied by broad changes in sediment supply and/or accommodation space within Gale crater. While the process by which the strata in the Lower formation of Mt. Sharp were deposited is still unknown, the morphological and mineralogical changes identified by *Milliken et al.* [2010], coupled with the systematic bed thickness changes identified here, can form the basis for depositional hypotheses testable in situ with the *Curiosity* rover [*Grotzinger et al.* 2012].

[69] RAM testing in Holden crater, west plateau of Juventae, and in Gale crater reveals that bed thickness in these sections is not randomly distributed about the mean, rather thin and thick beds tend to alternate frequently within the section (Table 4). RUD testing shows that Holden and Gale middle and upper member sections are consistent with a random ordering of bed thicknesses. However, a majority of the sections measured on the plateau west of Juventae are not random according to RUD testing. RUD testing uses the number of runs present in the section to determine whether or not an overall trend exists — too few runs suggests a trend and the null hypothesis of randomness is rejected. While this test is particularly sensitive to small-scale runs within the data that can obscure overall trends [*Chen and Hiscott*, 1999], the RUD results for the west plateau of Juventae are consistent with the overall thickening upward trends observed at this location. The testing performed here does not explain the specific mechanism responsible for the nonrandom distributions observed on the west plateau of Juventae, but the difference between the west Juventae plateau runs test results and those obtained in Holden and Gale may suggest that the process influencing deposition at Juventae is distinct from that at the other two study sites.

5.2.2. Statistical Distribution of Bed Thickness

[70] Cumulative frequency plots (Figure 14) show that lognormal distributions consistently provide the best fits to bed thickness frequencies in Holden crater. The results of Lilliefors testing support this observation (Table 5), as 8 of 10 Holden sections are statistically indistinguishable from a lognormal distribution at a 95% or greater significance level. *Talling* [2001] suggests that a lognormal bed thickness distribution represents a multiplicative addition of randomly distributed flow and sediment parameters. However, physical models that explain exactly how those parameters would produce a lognormal bed thickness distribution in a sedimentary sequence remain elusive. The lognormal distributions observed in Holden may represent the multiplicative combination of primary depositional variables, but additional modeling beyond the scope of this paper is needed to explore this possibility.

[71] Modal thickness is often interpreted to represent a recurrent response to some extrabasinal or intrabasinal periodic forcing function [i.e., *Lewis et al.*, 2008, and *Limaye et al.*, 2012]. If the lognormal distributions observed in Holden crater represent primary signals, the modal thickness between 20 and 60 cm observed in histograms may imply the recurrence of an as yet unknown process within the Holden depositional system that favored the formation of beds ~50 cm thick. Interestingly, Becquerel and Danielson, the two deposits previously identified as exhibiting cycling bedding [*Lewis et al.*, 2008, *Andrews-Hanna and Lewis*, 2011] reject both the normal and lognormal distributions in this study. In apparent conflict with these results, *Lewis et al.* [2008] observed a normal distribution in Becquerel crater, suggesting that a quasi-periodic process controlled by orbital variations was responsible for observed bed thickness ~4 m. A closer examination of the Becquerel histogram (Figure 3) reveals a minor mode at

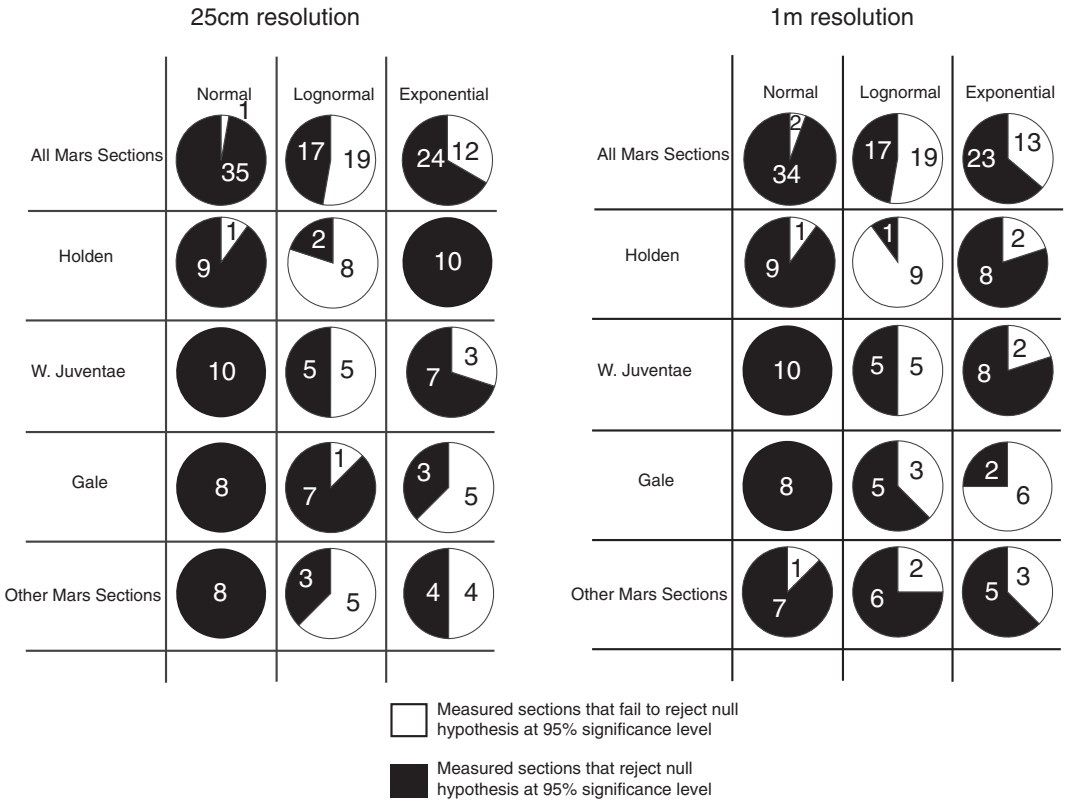

Figure 17. Pie charts showing the proportion of measured sections (measured on both 1 m and 25 cm orthoimages) for which the null hypothesis is rejected or failed to be rejected at a 95% significance level using the Lilliefors test.

~3 m, in addition to the most frequently populated bin <1 m. A minor mode is also present in the Danielson histogram at ~10 m. If a sampling bias is not responsible for the emergence of these modes (i.e., *Drummond and Wilkinson*, 1996), they could be representative of the cyclic processes suggested by *Lewis et al*. [2008] and *Andrews-Hanna and Lewis* [2011]. It is important to note that this study's results show the majority of beds in Becquerel and Danielson to be thinner than these minor modes, respectively, indicating that a previously unrecognized, small-scale, noncyclic process modulated deposition at these locations.

[72] Another explanation for the lognormal distributions observed in the Martian sections is the modification of some other input signal, such as a power-law or exponential distribution, due to "filtering" processes [*Malinverno*, 1997; *Carlson and Grotzinger*, 2001; *Jerolmack and Paola*, 2010] or sampling biases [*Drummond and Wilkinson*, 1996; *Rothman et al*., 1994]. Unfortunately, without a priori information about the depositional context, it is difficult, if not impossible, to distinguish the input distribution from the current distribution of bed thickness using only orbital measurements. Alternatively, *Drummond and Wilkinson* [1996] and *Rothman et al*. [1994] suggest that all lognormal bed thickness distributions are the result of a sampling bias that underrepresents thin beds in what should be negative exponential trends. Given that bed thickness was measured using orthoimages with resolution limits of 25 cm/pixel and 1 m/pixel, it is almost certain that beds exist at finer scales than can be measured here. For this reason, a sample bias cannot be rejected for either the 25 cm/pixel or 1 m/pixel sections examined in this study.

[73] Lognormal distributions are common in Holden crater, but lognormality is rejected for all but 1 section in the lower part of Mount Sharp in Gale crater and for 5 of the 10 sections measured on the west Juventae plateau. Additionally, sections measured on the west plateau of Juventae and in Gale crater rarely exhibit modal thickness (Figure 13). Theoretical exponential distributions provide reasonable fits to the west Juventae plateau and Gale sections (Figure 14), and 5 of the 8 Gale sections measured with the 25 cm/pixel orthoimages fail to reject the exponential distribution. These results suggest that bed thickness distributions in Gale and on the west Juventae plateau may be more consistent with stochastic sediment accumulation. In contrast to the bed thicknesses observed in the Lower formation, the Upper formation of Mount Sharp exhibits beds of very regular thickness [*Lewis*, 2009; *Milliken et al*., 2010; *Grotzinger and Milliken*, 2012], suggesting the influence of external forces not present in the deposition of lower mound materials. Bed thickness measurements with the *Curiosity* rover will likely provide additional insight to the observations made here, allowing a direct comparison of bed thicknesses derived from orbital observations to rover-based observations of bed thickness measurements and actual depositional processes.

5.2.3. Power-Law Behavior of Bed Thickness Frequency

[74] The log-log plots in Figure 15 show that bed thickness frequencies measured in Holden, on the plateau west of Juventae, and in Gale crater do not follow a power-law trend. The lack of power-law scaling in these deposits may rule out formation by sedimentary gravity flows or deposition

controlled by other scale-invariant processes. However, power-law scaling for many terrestrial turbidite deposits is supported by the occurrence of numerous thin beds that would be close to or below the resolution of HiRISE data. Because the number of thin beds decreases for most of these sections just above the resolution of HiRISE images, it is difficult to exclude power-law behavior entirely.

[75] The observed systematic change in power-law behavior with distance from the source in submarine fan deposits [*Carlson and Grotzinger*, 2001] suggests that characteristic modification of power-law behavior is linked to unique facies. Of all the sections measured in the study, those in Holden crater offer the best opportunity to observe systematic changes in power-law behavior with lateral facies variations because a sediment source (the crater wall) is known and the sections are arranged at increasing distance away from this source. However, systematic modification of power-law behavior is not observed from H1 to H10. This implies that the length scale of changes in fluvial/alluvial/lacustrine facies may be much longer than the length scale represented by the distance between H1 and H10. Alternatively, this may imply that some sediments in the measured beds were not sourced solely from the crater walls and may instead reflect alternative sources (e.g., evaporites, air-fall deposits, volcanic ash, etc.).

5.3. Building a Global Inventory of Bed Thickness Distributions on Mars

[76] In addition to the 28 total sections measured in Holden crater, on the plateau west of Juventae, and in Gale crater, sections were measured at seven other locations on Mars. Bed thickness statistics measured at different locations, even if for only 1 or 2 sections, can be used to build a global inventory of quantitative stratification characteristics. As an example, Figure 17 summarizes the Lilliefors test results of this study. Lognormal distributions are not ubiquitous for the sections measured here, but they are the most common distribution observed. Normal distributions are generally not observed in the Mars sections measured here, consistent with the observation of *Grotzinger and Milliken* [2012] that rhythmite deposits are rare on Mars. Exponential distributions are observed in Gale and at several other locations, but they appear to be less common than lognormal distributions.

[77] While this study builds the foundation for a global inventory of bed thickness, only 10 locations on the surface of Mars were analyzed. As a result, linking unique depositional environments with specific bed thickness distributions is difficult. However, there are a number of ways by which depositional environments or mechanisms could be linked to unique bed thickness statistics in the future. For example, dozens of large alluvial fans have been identified in highland craters on Mars [*Moore and Howard*, 2005]. If DTMs were produced and bed thickness distributions measured for the dozens of observed alluvial fan deposits, trends in bed thickness could lead to the development of facies-specific criteria. These criteria would have the potential to distinguish alluvial deposits globally on Mars, particularly in outcrops where morphological characteristics may be ambiguous, i.e., crater-filling mounds. Another example could be the systematic study of bed thickness distributions in the interior layered deposits of Valles Marineris, a number of which are known to contain sulfates [*Gendrin et al*., 2005; *Mangold et al*., 2008]. Comparison of bed thickness properties of these deposits to those observed in locations such as Danielson could provide an independent test as to whether these deposits have similar origins, as has been suggested based on mineralogical data [*Arvidson et al*., 2005; *Bibring et al*., 2007]. Future work could also include a systematic study of bed thickness statistics in deposits exhibiting distinct orbital mineralogy [*Bibring et al*., 2006], comparing bed thickness in phyllosilicate-bearing deposits [*Poulet et al*., 2005; *Bibring et al*., 2006] with those measured in sulfate-bearing terrains [*Gendrin et al*., 2005].

5.4. Challenges of Bed Thickness Analysis

[78] Although the analysis of bed thickness statistics and distributions holds much promise in helping to illuminate the depositional history of sedimentary rocks on Mars, there are numerous challenges associated with this type of analysis.

[79] For many, if not most, of the sedimentary deposits on Mars, there exists limited a priori knowledge of the processes, conditions, or forcing mechanisms that produced the changes in brightness that are identified as beds. It is generally assumed that the bedding planes primary depositional surfaces [*Grotzinger and Milliken*, 2012], but there is considerable uncertainty about the expression of depositional versus diagenetic signals, intrinsic organization versus external forcing, and what length hiatus, if any, bed boundaries signify. However, it is this uncertainty that necessitates bed thickness analyses like that presented in this study. Unlike on Earth, where outcrops and rocks can be examined in the field and laboratory in great detail to fully test depositional hypotheses, studies on Mars are currently (and for the foreseeable future) forced to rely on satellite as well as rare rover and lander observations. In this context, it is prudent to consider all observations that can be accurately measured and quantified in order to fully characterize depositional environments and processes on Mars. Even if bed thickness is a non-unique parameter and if the specific mechanisms that give rise to bedding are unknown, it still remains one of the few properties of Martian strata that can be quantified and approached from a statistical vantage point with existing orbital data. Bed thickness alone is likely not sufficient to uniquely determine a depositional environment, but it is an important characteristic of sedimentary strata that should be integrated with other observations when documenting and describing a stratigraphic section. Parameters such as mean bed thickness, range in thickness, and thickening/thinning upward trends are probably most useful when integrated with additional statistical, stratigraphic, and compositional analyses.

[80] The resolution limits of orbital data pose a major challenge when attempting to extract depositional information from bed thickness measurements on Mars. This study uses 25 cm orthophotos draped on 1 m DTMs to identify and measure bed thickness, thereby requiring oversampling of the 1 m DTM to obtain elevation values for the observed bed boundaries. By interpolating between tiepoints, it is possible to measure the thickness of very thin beds visible in the 25 cm orthoimages, but oversampling can result in very large relative errors in thickness. This is the case for many of the Holden thickness measurements (Figure 9) where the error of individual thickness measurements is dominated by the vertical precision of the DTM. Averaging individual

thickness measurements for each section helps reduce the overall error and enables comparison between sections, but large errors make identification of trends within each section difficult. Additionally, beds whose thickness is at or near the resolution of orbital data are particularly susceptible to the effects of slope on DTM and orthoimage resolution. Sections measured in this study generally do not show significant changes in slope upsection (Figure A1; Athabasca, Danielson, and Candor1 sections are exceptions), so this effect is likely minimal here. It is acknowledged, however, that comparisons between very thinly bedded sections with different slopes could be susceptible to this effect.

[81] It is also possible that the beds identified in orbital images consist of amalgamated thinner beds that are simply below image resolution. In addition, the quality of outcrop exposure may affect the scale of observable bedding as thinner beds can be obscured by dust or other surficial deposits. Disruption of an outcrop by post-depositional deformation, such as impact cratering, may also obscure in orbital imagery. These factors may result in an underrepresentation of thin beds in the histograms, CF plots, and log-log plots presented here, affecting the ability to detect lateral or vertical thinning or thickening trends. The effects of resolution are most apparent in this study when comparing the 25 cm and 1 m data sets. The main trends in runs testing and distribution fits are generally similar between the 25 cm and 1 m data sets, but statistical testing of specific sections sometimes fails to produce the same results at both resolutions. Disparities in the thinning and thickening trends identified in Holden and on the west plateau of Juventae in the 25 cm/pixel and 1 m/pixel data sets are examples of this (Figures 9 and 10 and Table A2). Therefore, it is important to consider that the techniques presented in this study can only interrogate bedding and depositional processes down to a scale defined by image resolution. Scales of deposition representing the thinnest beds and finest-scale processes simply cannot be studied with these remote methods.

[82] In studies of turbidite bed thickness on Earth, it is usually possible to measure hundreds to thousands of beds. On Mars, the number of beds that can be measured in an outcrop is constrained by a number of factors, including the extent and quality of outcrop exposure and the outcrop slope. A sample size of $n = 30$ typically separates large-sample statistics from small-sample statistics, and below this size sampling uncertainties become important [*Davis*, 2002]. The number of beds measured in several of the sections presented here is just at or below the small-sample statistic boundary and still significantly less than the number of beds measured in Earth studies. Additionally, when only one section is measured at a location, it is difficult to determine whether the statistical results are truly representative of the deposit. Therefore, Martian deposits must contain a certain number of beds, the more the better, to avoid small-sample statistical uncertainties, and it is prudent to measure as many sections as possible in a particular location.

[83] Because of the uncertainties and limitations associated with using bed thickness to study sedimentary deposits on Mars, it is unrealistic to expect that thickness measurements and frequency distributions will reveal unique depositional mechanisms and environments for all sedimentary sequences. The application of bed thickness analysis on Earth has been limited largely to specific facies, mostly commonly deep-water turbidites and shallow marine carbonates. A statistically significant number of bed thickness distributions simply has not been compiled for enough sedimentary deposits on Earth (e.g., pyroclastic deposits, alluvial fans, fluvial systems, evaporite sequences) to know if bed thickness alone can uniquely represent a particular depositional process or environment. Additional work is needed on both Earth and Mars to link specific statistical distributions, deviations from those distributions, and characteristic bed thickness to depositional processes and environments.

6. Conclusions

[84] By necessity, previous studies of sedimentary deposits and environments on Mars have been grounded in qualitative geomorphological observations. Although such observations are powerful, the hypotheses that derive from such observations must ultimately be tested by actual measurements or models. For the first time, high-resolution DTMs such as those derived from HiRISE images provide the opportunity to quantify bed thickness properties down to the submeter scale. This study highlights ways that statistical techniques can enhance understanding of depositional processes and environments on Mars. For example, relatively constant bed thicknesses observed in Holden crater and on the plains west of Juventae Chasma favor deposition by fallout processes common in lacustrine and air-fall deposits. Meanwhile, the exponential distributions observed in the lower Mt. Sharp suggest stochastic deposition at odds with rhythmic trends observed higher up in the sequence at Gale crater. The Becquerel-Danielson analysis illustrates the usefulness of statistical bed thickness analysis in several ways. First, it allows for a quantitative comparison between two spatially distinct locations on Mars, highlighting similarities and differences between the two deposits beyond what is apparent from qualitative morphological observations. Additionally, the methods presented here provide insight into a small-scale aperiodic depositional process previously unrecognized in a region of Mars known for its cyclic sedimentation. Although the likely non-uniqueness of bed thickness distributions and the limitations imposed by the resolution of the data are acknowledged, the statistical analysis of bed thickness provides a more objective and quantitative approach to the characterization of Martian strata while also aiding in the study of sedimentary depositional processes. This statistical approach can now be applied to the increasing number of layered deposits imaged on Mars, building a global inventory of quantitative stratigraphic properties.

Notation

a scaling constant in exponential equation
α angle between the measured section and the dip direction, degrees
b scaling constant in exponential equation
c scaling constant in power-law equation
d constant scaling exponent in power-law equation given by slope of the plot in $\log(N)$ versus $\log(t)$ space
δ dip of beds, degrees

e	emission angle, angle between a line extending from the center of a HiRISE image to the spacecraft and a "normal" perpendicular to the planet's surface, degrees
g	rate parameter of an exponential distribution
EP	expected vertical precision of DTM
GSD	ground sample distance, meter/pixel resolution of the more oblique image in the HiRISE image pair, *m*
h	horizontal distance along the measured section line between the upper and lower bed boundaries, *m*
H_0	null hypothesis
n	number of beds in a section
N	number of beds as a function of thickness t
ρ	pixel matching error of a stereo pair
p	significance probability
P	parallax, degrees
σ	standard deviation of bed thickness, *m*
t	bed thickness, *m*
μ	mean bed thickness, *m*
v	elevation difference between upper and lower boundaries of each bed, *m*

[86] **Acknowledgments.** This work was supported by NASA grant NAS7-03001. We thank J. Metz, A. Hayes, A. Limaye, and S. Mattsen for their helpful comments and discussion. Reviews by N. Mangold, Laeticia Le Deit, and an anonymous reviewer helped improve this manuscript.

References

Anderson, R. B., and J. F. Bell (2010), Geologic mapping and characterization of Gale Crater and implications for its potential as a Mars Science Laboratory landing site, *Mars*, 5, 76–128, doi:10.1555/mars.2010.0004.

Andrews-Hanna J. C., and K. W. Lewis (2011), Early Mars Hydrology: 2. Hydrological evolution in the Noachian and Hesperian Epochs, *J. Geophys. Res.*, 116, E02007, doi:10.1029/2010JE003709.

Arvidson, R. E., F. Poulet, J.-P. Bibring, M. Wolff, A. Gendrin, R. V. Morris, J. J. Freeman, Y. Langevin, N. Mangold, and G. Bellucci (2005), Spectral Reflectance and Morphologic Correlations in Eastern Terra Meridiani, Mars, *Science*, 307(5715), 1591–1594, doi:10.1126/science.1109509.

Atkinson, D. J. (1962), Tectonic Control of Sedimentation and the Interpretation of Sediment Alternation in the Tertiary of Prince Charles Foreland, Spitsbergen, *Geol. Soc. Am. Bull.*, 73(3), 343–364, doi:10.1130/0016-7606(1962)73[343:TCOSAT]2.0.CO;2.

Awadallah, S. A. M., R. N. Hiscott, M. Bidgood, and T. E. Crowther (2001), Turbidite facies and bed-thickness characteristics inferred from microresistivity (FMS) images of Lower to Upper Pliocene rift-basin deposits, Woodlark Basin, offshore Papua New Guinea, in *Proc. ODP, Science Results*, vol. 180, edited by P. Huchon, et al., pp. 1–29, ODP, College Station, TX, doi:10.2973/odp.proc.sr.180.166.2001.

Banks, M. E., N. P. Lang, J. S. Kargel, A. S. McEwen, V. R. Baker, J. A. Grant, J. D. Pelletier, and R. G. Strom (2009), An analysis of sinuous ridges in the southern Argyre Planitia, Mars using HiRISE and CTX images and MOLA data, *J. Geophys. Res.*, 114(E9), E09003, doi:10.1029/2008JE003244.

Beattie, P. D., and W. B. Dade (1996), Is scaling in turbidite deposition consistent with forcing by earthquakes?, *J. Sediment. Res.*, 66(5), 909–915, doi:10.1306/D4268437-2B26-11D7-8648000102C1865D.

Bhattacharya, J. P., T. H. D. Payenberg, S. C. Lang, and M. Bourke (2005), Dynamic river channels suggest a long-lived Noachian crater lake on Mars, *Geophys. Res. Lett.*, 32, L10201, doi:10.1029/2005GL022747.

Bibring, J.-P., et al. (2006), Global Mineralogical and Aqueous Mars History Derived from OMEGA/Mars Express Data, *Science*, 312, doi:10.1126/science.1122659.

Bibring, J.-P., et al. (2007), Coupled ferric oxides and sulfates on the Martian surface, *Science*, 317, 1206–1210, doi:10.1126/science.1144174.

Bishop, J. L., et al. (2009), Mineralogy of Juventae Chasma: Sulfates in the light-toned mounds, mafic minerals in the bedrock, and hydrated silica and hydroxylated ferric sulfate on the plain, *J. Geophys. Res.*, 114, E00D09, doi:10.1029/2009JE003352.

Blackwelder, E., and H. H. Barrows (1911), *Elements of Geology*, American Book Company, New York, NY, pp. 475.

Burgess, P. M. (2008), The nature of shallow-water carbonate lithofacies thickness distributions, *Geology*, 36(3), 235–238, doi:10.1130/G243326A.1.

Burr, D. M. (2003), Hydraulic modelling of Athabasca Vallis, Mars, *Hydrolog. Sci. J.*, 48(4), 655–664, doi:10.1623/hysj.48.4.655.51407.

Burr, D. (2005), Clustered streamlined forms in Athabasca Valles, Mars: Evidence for sediment deposition during floodwater ponding, *Geomorphology*, 69(1–4), 242–252, doi:10.1016/j.geomorph.2005.01.009.

Cadieux, S. B. (2011), Constraining martian sedimentation via analysis of stratal packaging, intracrater layered deposits, Arabia Terra, Mars, M. Sc. dissertation, University of Tennessee, Knoxville, Tenn.

Carlson, J., and J. P. Grotzinger (2001), Submarine fan environment inferred from turbidite thickness distributions, *Sedimentology*, 48(6), 1331–1351, doi:10.1046/j.1365-3091.2001.00426.x.

Carr, M. H. (1996), *Water on Mars*, p. 248, Oxford University Press, New York.

Chen, C., and R. N. Hiscott (1999), Statistical analysis of turbidite cycles in submarine fan successions; tests for short-term persistence, *J. Sediment. Res.*, 69(2), 486–504.

Christie-Blick, N., and N. W. Driscoll (1995), Sequence Stratigraphy, *Annu. Rev. Earth Planet. Sci.*, 23, 451–478, doi:10.1146/annurev.earth.23.1.451.

Cutts, J. A. (1973), Nature and Origin of Layered Deposits of the Martian Polar Regions, *J. Geophys. Res.*, 78(20), 4231–4249, doi:10.1029/JB078i020p04231.

Davis, J. C. (2002), *Statistics and Data Analysis in Geology*, John Wiley & Sons, New York, NY, 3rd edition, pp. 638 .

Drummond, C. N., and B. H. Wilkinson (1996), Statal thickness frequencies and the prevalence of orderedness in stratigraphic sequences, *J. Geol.*, 104(1), 1–18, doi:10.1086/629798.

Edgett, K. S. (2005), The sedimentary rocks of Sinus Meridiani: Five key observations from data acquired by the Mars Global Surveyor and Mars Odyssey orbiters, *Mars*, 1, 5–58, doi:10.1555/mars.2005.0002.

Edgett, K. S., and M. C. Malin (2002), Martian sedimentary rock stratigraphy: Outcrops and interbedded craters of northwest Sinus Meridiani and southwest Arabia Terra, *Geophys. Res. Lett.*, 29(24), 2179, doi:10.1029/2002GL016515.

Fischer, A. G. (1964) The Lofer cyclothems of the Alpine Triassic, in *Symposium on Cyclic Sedimentation*, vol. 169, edited by D. R. Merriam, pp. 107–149, KGS, Univ. of Kansas, Lawrence, Kan.

Fishbaugh, K. E., S. Byrne, K. E. Herkenhoff, R. L. Kirk, C. Fortezzo, P. S. Russell, and A. McEwen (2010a), Evaluating the meaning of "layer" in the Martian north polar layered deposits and the impact on the climate connection, *Icarus*, 205(1), 269–282, doi:10.1016/j.icarus.2009.04.011.

Fishbaugh, K. E., C. S. Hvidberg, S. Byrne, P. S. Russell, K. E. Herkenhoff, M. Winstrup, and R. Kirk (2010b), First high-resolution stratigraphic column of the Martian north polar layered deposits, *Geophys. Res. Lett.*, 37, L07201, doi:10.1029/2009GL041642.

Flemings, P. B. and J. P. Grotzinger (1996), STRATA: Freeware for analyzing classic stratigraphic problems, *GSA Today*, 6(12).

Fueten, F., R. Stesky, P. MacKinnon, E. Hauber, T. Zegers, K. Gwinner, F. Scholten, and G. Neukum (2008), Stratigraphy and structure of interior layered deposits in west Candor Chasma, Mars, from High Resolution Stereo Camera (HRSC) stereo imagery and derived elevations, *J. Geophys. Res.*, 113, E10008, doi:10.1029/2007JE003053.

Fueten, F., R. Harvy, R. Stesky, E. Hauber, A. Rossi, and N. Mangold (2011), Layer thickness determination of interior layered deposits, with particular emphasis on Candor Mensa, Mars, Lunar Planet. Sci., XLII, Abstract 1255.

Gendrin, A., et al. (2005), Sulfates in Martian Layered Terrains: The OMEGA/Mars Express View, *Science*, 307(5715), 1587–1591, doi:10.1126/science.1109087.

Grant, J. A., R. P. Irwin, J. P. Grotzinger, R. E. Milliken, L. L. Tornabene, A. S. McEwen, C. M. Weitz, S. W. Squyres, T. D. Glotch, and B. J. Thomson (2008), HiRISE imaging of impact megabreccia and submeter aqueous strata in Holden Crater, Mars, *Geology*, 36(3), 195–198, doi:10.1130/G24340A.1.

Grant, J. A., R. P. Irwin III, S. A. Wilson, D. Buczkowski, and K. Siebach (2011), A lake in Uzboi Vallis and implications for Late Noachian-Early Hesperian climate on Mars, *Icarus*, *212*(1), 110–122, doi:10.1016/j.icarus.2010.11.024.

Groshong, R. H., Jr. (1999), *3-D Structural Geology*, p. 324, Springer, New York.

Grotzinger, J. P. and R. E. Milliken (2012), The sedimentary rock record of Mars: Distribution, origins, and global stratigraphy, in *Sedimentary Geology of Mars*, SEPM Special Publication No. 102, edited by J. P. Grotzinger and R. E. Milliken, pp. 1–48, SEPM, Tulsa, O. K.

Grotzinger, J. P., et al. (2005), Stratigraphy and sedimentology of a dry to wet eolian depositional system, Burns formation, Meridiani Planum, Mars, *Earth Planet. Sci. Lett.*, 240(1), 11–72, doi:10.1016/j.epsl.2005.09.039.

Grotzinger, J., D. Beatty, G. Dromart, S. Gupta, M. Harris, J. Hurowitz, G. Kocurek, S. McLennan, R. E. Milliken, G. Ori, and D. Sumner (2011), The sedimentary record of Mars, *The Sedimentary Record*, 9(2), 4–8, doi:10.2110/sedred/2011.2.4.

Grotzinger, J., et al. (2012), Mars Science Laboratory Mission and Science Investigation, *Space Sci. Rev.*, 170(1–4), 5–56, doi:10.1007/s11214-012-9892-2.

Hiesinger, H., and J. W. Head III (2002), Topography and morphology of the Argyre Basin, Mars: implications for its geologic and hydrologic history, *Planet. Space Sci.*, 50(10–11), 939–981, doi:10.1016/S0032-0633(02)00054-5.

Hinnov, L. A., and R. K. Goldhammer (1991), Spectral analysis of the Middle Triassic Latemar Limestone, *J. Sediment. Res.*, 61(7), 1173–1193, doi:10.1306/D4267861-2B26-11D7-8648000102C1865D.

Howard, A. D. (1981), Etched plateau and braided ridges of the south polar region of Mars: Features produced by melting of ground ice?, in Reports of Planetary Geology Program-1981, NASA Tech. Memo, 84211, pp. 286–289, NASA Office of Space Science, Washington, D.C.

Jaeger, W. L., L. P. Keszthelyi, A. S. McEwen, C. M. Dundas, and P. S. Russell (2007), HiRISE observations of Athabasca Valles, Mars: A lava-draped channel system, *Science*, 317(5845), 1709–1711, doi:10.1126/science.1143315.

Jaeger, W. L., L. P. Keszthelyi, J. A. Skinner Jr, M. P. Milazzo, A. S. McEwen, T. N. Titus, M. R. Rosiek, D. M. Galuszka, E. Howington-Kraus, and R. L. Kirk (2010), Emplacement of the youngest flood lava on Mars: A short, turbulent story, *Icarus*, 205(1), 230–243, doi:10.1016/j.icarus.2009.09.011.

Jaumann, R., et al. (2007), The high-resolution stereo camera (HRSC) experiment on Mars Express: Instrument aspects and experiment conduct from interplanetary cruise through the nominal mission, *Planet. Space Sci.*, 55(7–8), 928–952, doi:10.1016/j.pss.2006.12.003.

Jerolmack, D. J., and C. Paola (2010), Shredding of environmental signals by sediment transport, *Geophys. Res. Lett.*, 37, L19401, doi:10.1029/2010GL044638.

Kargel, J. S., and R. G. Strom (1992), Ancient glaciation on Mars, *Geology*, 20(1), 3–7, doi:10.1130/0091-7613(1992)020<0003:AGOM>2.3.CO;2.

Kirk, R. L., et al. (2008), Ultrahigh resolution topographic mapping of Mars with MRO HiRISE stereo images: Meter-scale slopes of candidate Phoenix landing sites, *J. Geophys. Res.*, 113, E00A24, doi:10.1029/2007JE003000.

Koch, G. S., and R. F. Link (1980), *Statistical Analysis of Geological Data,* 832 pp, Dover Publications, Inc., Mineola, NY.

Lang, H. R., S. L. Adams, J. E. Conel, B. A. McGuffie, E. D. Paylor, R. E. Walker (1987), Multispectral Remote Sensing as Stratigraphic and Structural Tool, Wind River Basin and Big Horn Basin Areas, Wyoming, *AAPG Bulletin*, 71(4), 389–402.

Laskar, J., B. Levrard, and J. F. Mustard (2002), Orbital forcing of the Martian polar layered deposits, *Nature*, 419(6905), 375–377, doi:10.1038/nature01066.

Le Deit, L., O. Bourgeois, D. Mège, E. Hauber, S. Le Mouélic, M. Massé, R. Jaumann, and J. P. Bibring (2010), Morphology, stratigraphy, and mineralogical composition of a layered formation covering the plateaus around Valles Marineris, Mars: Implications for its geological history, *Icarus*, 208(2), 684–703, doi:10.1016/j.icarus.2010.03.012.

Leverington, D. W. (2004), Volcanic rilles, streamlined islands, and the origin of outflow channels on Mars, *J. Geophys. Res.*, 109, E10011, doi:10.1029/2004JE002311.

Lewis, K. W. (2009), The rock record of Mars: structure, sedimentology and stratigraphy, Ph.D. dissertation, Dept. of Geol. and Planet. Sci., Caltech, Pasadena, CA.

Lewis, K. W., and O. Aharonson (2006), Stratigraphic analysis of the distributary fan in Eberswalde crater using stereo imagery, *J. Geophys. Res.*, 111, E06001, doi:10.1029/2005JE002558.

Lewis, K. W., O. Aharonson, J. P. Grotzinger, R. L. Kirk, A. S. McEwen, and T.-A. Suer (2008), Quasi-Periodic Bedding in the Sedimentary Rock Record of Mars, *Science*, 322(5907), 1532–1535, doi:10.1126/science.1161870.

Lewis, K. W., O. Aharonson, J. P. Grotzinger, A. S. McEwen, and R. L. Kirk (2010), Global significance of cyclic sedimentary deposits on Mars, Lunar Planet. Sci., XLI, Abstract 2648.

Lilliefors, H. W. (1967), On the Kolmogorov-Smirnov Test for Normality with Mean and Variance Unknown, *J. Am. Stat. Assoc.*, 62(318), 399–402.

Lilliefors, H. W. (1969), On the Kolmogorov-Smirnov Test for the Exponential Distribution with Mean Unknown, *J. Am. Stat. Assoc.*, 64(325), 387–389.

Limaye, A. B. S., O. Aharonson, and J. T. Perron (2012), Detailed stratigraphy and bed thickness of the Mars north and south polar layered deposits, *J. Geophys. Res.*, 117, E06009, doi:10.1029/2011JE003961.

Lowey, G. W. (1992), Variation in bed thickness in a turbidite succession, Dezadeash Formation (Jurassic-Cretaceous), Yukon, Canada: evidence of thinning-upward and thickening-upward cycles, *Sediment. Geol.*, 78(3–4), 217–232, doi:10.1016/0037-0738(92)90021-i.

Lucchitta, B. K., A. S. McEwen, G. D. Clow, P. E. Geissler, R. B. Singer, R. A. Schutz, S. W. Squyres (1992), The canyon system of Mars, in *Mars*, edited by H. H. Kieffer, et al., pp. 453–492, University of Arizona Press, Tucson.

Malin, M. C., and K. S. Edgett (2000), Sedimentary Rocks of Early Mars, *Science*, 290(5498), 1927–1937, doi:10.1126/science.290.5498.1927.

Malin, M. C., and K. S. Edgett (2001), Mars Global Surveyor Mars Orbiter Camera: Interplanetary cruise through primary mission, *J. Geophys. Res.*, 106(E10), 23429–23570, doi:10.1029/2000JE001455.

Malinverno, A. (1997), On the power law size distribution of turbidite beds, *Basin Res.*, 9(4), 263–274, doi:10.1046/j.1365-2117.1997.00044.x.

Mangold, N., A. Gendrin, B. Gondet, S. LeMouelic, C. Quantin, V. Ansan, J.-P. Bibring, Y. Langevin, P. Masson, and G. Neukum (2008), Spectral and geological study of the sulfate-rich region of West Candor Chasma, Mars, *Icarus*, 194(2), 519–543, doi:10.1029/2008JE003245.

McEwen, A. S., et al. (2010), The High Resolution Imaging Science Experiment (HiRISE) during MRO's Primary Science Phase (PSP), *Icarus*, 205(1), 2–37, doi:10.1016/j.icarus.2009.04.023.

Metz, J. M. (2010), A study of the record of ancient sedimentary rocks on Mars using MER, HiRISE, and CRISM images, Ph.D. dissertation, Dept. of Geol. and Planet. Sci., Caltech, Pasadena, CA.

Metz, J., J. Grotzinger, C. Okubo, and R. Milliken (2010), Thin-skinned deformation of sedimentary rocks in Valles Marineris, Mars, *J. Geophys. Res.*, *115*(E11), E11004, doi:10.1029/2010je003593.

Milkovich, S. M., and J. W. Head, III (2005), North polar cap of Mars: Polar layered deposit characterization and identification of a fundamental climate signal, *J. Geophys. Res.*, 110, E01005, doi:10.1029/2004JE002349.

Milliken, R. E., and D. L. Bish (2010), Sources and sinks of clay minerals on Mars, *Phil. Mag.*, 90(17–18), 2293–2308, doi:10.1080/14786430903575132.

Milliken, R. E., et al. (2008), Opaline silica in young deposits on Mars, *Geology*, 36(11), 847–850, doi:10.1130/G24967A.

Milliken, R. E., J. P. Grotzinger, and B. J. Thomson (2010), Paleoclimate of Mars as captured by the stratigraphic record in Gale Crater, *Geophys. Res. Lett.*, 37, L04201, doi:10.1029/2009GL041870.

Mitchum, R. M., Jr., and P. R. Vail (1977), Seismic stratigraphy and global changes of sea-level, Part 7: Stratigraphic interpretation of seismic reflection patterns in depositional sequences, in *Seismic Stratigraphy-Applications to Hydrocarbon Exploration*, AAPG Special Volumes, vol. M 26, edited by C. E. Payton, pp.135–144, AAPG, Tulsa, OK.

Moore, J. M., and A. D. Howard (2005), Large alluvial fans on Mars, *J. Geophys. Res.*, 110, E04005, doi:10.1029/2004je002352.

Moore, J. M., A. D. Howard, W. E. Dietrich, and P. M. Schenk (2003), Martian Layered Fluvial Deposits: Implications for Noachian Climate Scenarios, *Geophys. Res. Lett.*, 30(24), 2292, doi:10.1029/2003GL019002.

Murchie, S., et al. (2009), Evidence for the origin of layered deposits in Candor Chasma, Mars, from mineral composition and hydrologic modeling, *J. Geophys. Res.*, 114, E00D05, doi:10.1029/2009JE003343.

Murray, B. C., L. A. Soderblom, J. A. Cutts, R. P. Sharp, D. J. Milton, and R. B. Leighton (1972), Geological framework of the south polar region of Mars, *Icarus*, 17(2), 328–345, doi:10.1016/0019-1035(72)90004-8.

Neukum, G., et al. (2004), Recent and episodic volcanic and glacial activity on Mars revealed by the High Resolution Stereo Camera, *Nature*, 432(7020), 971–979, doi:10.1038/nature03231.

Okubo, C. H. (2010), Structural geology of Amazonian-aged layered sedimentary deposits in southwest Candor Chasma, Mars, *Icarus*, 207(1), 210–225, doi:10.1016/j.icarus.2009.11.012.

Okubo, C. H., and A. S. McEwen (2007), Fracture-Controlled Paleo-Fluid Flow in Candor Chasma, Mars, *Science*, 315(5814), 983–985, doi:10.1126/science.1136855.

Parker, T. J., D. C. Pieri, and R. S. Saunders (1986), Morphology and distribution of sinuous ridges in central and southern Argyre, in *Reports of the Planetary Geology and Geophysics Program*, NASA Tech. Memo, 88383, pp. 468–470, NASA Office of Space Sci., Washington, D.C.

Pondrelli, M., A. Baliva, S. Di Lorenzo, L. Marinangeli, and A. P. Rossi (2005), Complex evolution of paleolacustrine systems on Mars: An example from the Holden crater, *J. Geophys. Res.*, 110, E04016, doi:10.1029/2004JE002335.

Pondrelli, M., A. P. Rossi, L. Marinangeli, E. Hauber, K. Gwinner, A. Baliva, and S. Di Lorenzo (2008), Evolution and depositional environments of the Eberswalde fan delta, Mars, *Icarus*, 197(2), 429–451, doi:10.1016/j.icarus.2008.05.018.

Poulet, F., J.-P. Bibring, J. F. Mustard, A. Gendrin, N. Mangold, Y. Langevin, R. E. Arvidson, B. Gondet, and C. Gomez (2005), Phyllosilicates on Mars and Implications for early Martian climate, *Nature*, 438, doi:10.1038/nature04274.

Read, J. F., and R. K. Goldhammer (1988), Use of Fischer plots to define third-order sea-level curves in Ordovician peritidal cyclic carbonates, Appalachians, *Geology*, 16(10), 895–899, doi:10.1130/0091-7613(1988)016<0895:UOFPTD>2.3.CO;2.

Ricci Lucchi, F. (1969), Channelized deposits in the Middle Miocene flysch of Romagna (Italy), *Giorn. Geol.*, 36(2), 203–282.

Rice, J. W., Jr., P. R. Christensen, S. W. Ruff, and J. C. Harris (2003), Martian fluvial landforms: a THEMIS perspective after one year at Mars, Lunar Planet. Sci., XXXIV, Abstract 2091.

Rothman, D. H., and J. P. Grotzinger (1995), Scaling properties of gravity-driven sediments, *Nonlin. Process. Geophys.*, 2(3–4), 178–185, doi:10.5194/npg-2-178-1995.

Rothman, D. H., J. P. Grotzinger, and P. Flemings (1994), Scaling in turbidite deposition, *J. Sediment. Res.*, 64(1a), 59–67, doi:10.1306/D4267D07-2B26-11D7-8648000102C1865D.

Sadler, P. M. (1981), Sediment accumulation rates and the completeness of stratigraphic sections, *J. Geol.*, 89(5), 569–584, doi:10.1086/628623.

Scott, D. H. and K. L. Tanaka (1986), Geologic Map of the Western Equatorial Region of Mars: U.S. Geological Survey, Flagstaff, AZ.

Sgavetti, M., M. Carla Ferrari, R. Chiari, P. L. Fantozzi, and I. Longhi (1995), Stratigraphic Correlation by Integrating Photostratigraphy and Remote Sensing Multispectral Data: An Example from Jurassic-Eocene Strata, Northern Somalia, *AAPG Bulletin*, 79(11), 1571–1589.

Sharp, R. P. (1973), Mars: Troughed Terrain, *J. Geophys. Res.*, 78(20), 4063–4072, doi:10.1029/JB078i020p04063.

Sloss, L. L. (1963), Sequences in the Cratonic Interior of North America, *Geol. Soc. Am. Bull.*, 74(2), 93–114, doi:10.1130/0016-7606(1963)74[93:SITCIO]2.0.CO;2.

Smith, D. E., et al. (2001), Mars Orbiter Laser Altimeter: Experiment summary after the first year of global mapping of Mars, *J. Geophys. Res.*, 106(E10), 23689–23722, doi:10.1029/2000JE001364.

Snyder, C. W. (1979), The extended mission of Viking, *J. Geophys. Res.*, 84(B14), 7917–7933, doi:10.1029/JB084iB14p07917.

Soderblom, L. A., M. C. Malin, J. A. Cutts, and B. C. Murray (1973), Mariner 9 Observations of the Surface of Mars in the North Polar Region, *J. Geophys. Res.*, 78(20), 4197–4210, doi:10.1029/JB078i020p04197.

Squyres, S. W., et al. (2004), In Situ Evidence for an Ancient Aqueous Environment at Meridiani Planum, Mars, *Science*, 306(5702), 1709–1714, doi:10.1126/science.1104559.

Squyres, S. W., et al. (2007), Pyroclastic Activity at Home Plate in Gusev Crater, Mars, *Science*, 316(5825), 738–742, doi:10.1126/science.1139045.

Sylvester, Z. (2007), Turbidite bed thickness distributions: methods and pitfalls of analysis and modelling, *Sedimentology*, 54(4), 847–870, doi:10.1111/j.1365-3091.2007.00863.x.

Talling, P. J. (2001), On the frequency distribution of turbidite thickness, *Sedimentology*, 48(6), 1297–1329, doi:10.1046/j.1365-3091.2001.00423.x.

Tanaka, K. L. (1986), The Stratigraphy of Mars, *J. Geophys. Res.*, 91(B13), E139–E158, doi:10.1029/JB091iB13p0E139.

Thomson, B. J., N. T. Bridges, R. Milliken, A. Baldridge, S. J. Hook, J. K. Crowley, G. M. Marion, C. R. de Souza Filho, A. J. Brown, and C. M. Weitz (2011), Constraints on the origin and evolution of the layered mound in Gale Crater, Mars using Mars Reconnaissance Orbiter data, *Icarus*, 214(2), 413–432, doi:10.1016/j.icarus.2011.05.002.

Watters, W. A., J. P. Grotzinger, J. Bell III, J. Grant, A. G. Hayes, R. Li, S. W. Squyres, and M. T. Zuber (2011), Origin of the structure and planform of small impact craters in fractured targets: Endurance Crater at Meridiani Planum, Mars, *Icarus*, 211(1), 472–497, doi:10.1016/j.icarus.2010.08.030.

Weitz, C. M., R. E. Milliken, J. A. Grant, A. S. McEwen, R. M. E. Williams, and J. L. Bishop (2008), Light-toned strata and inverted channels adjacent to Juventae and Ganges chasmata, Mars, *Geophys. Res. Lett.*, 35(19), L19202, doi:10.1029/2008GL035317.

Weitz, C. M., R. E. Milliken, J. A. Grant, A. S. McEwen, R. M. E. Williams, J. L. Bishop, and B. J. Thomson (2010), Mars Reconnaissance Orbiter observations of light-toned layered deposits and associated fluvial landforms on the plateau adjacent to Valles Marineris, *Icarus*, 205(1), 73–102, doi:10.1016/j.icarus.2009.04.017.

Wheeler, H. E. (1958), Time-stratigraphy, *AAPG Bulletin*, 42(5), 1047–1063.

Wheeler, H. E. (1959), Unconformity-bounded units in stratigraphy, Note 24 of American Commission on Stratigraphic Nomenclature, *AAPG Bulletin*, 43(8), 1975–1977, doi:10.1306/0BDA5E85-16BD-11D7-8645000102C1865D.

Wilkinson, B. H., and C. N. Drummond (2004), Facies Mosaics Across the Persian Gulf and Around Antigua—Stochastic and Deterministic Products of Shallow-Water Sediment Accumulation, *J. Sediment. Res.*, 74(4), 513–526, doi:10.1306/123103740513.

Wilkinson, B. H., C. N. Drummond, E. D. Rothman, and N. W. Diedrich (1997), Stratal order in peritidal carbonate sequences, *J. Sediment. Res.*, 67(6), 1068–1082, doi:10.1306/D42686CB-2B26-11D7-8648000102C1865D.

Wilkinson, B. H., C. N. Drummond, N. W. Diedrich, and E. D. Rothman (1999), Poisson processes of carbonate accumulation on Paleozoic and Holocene platforms, *J. Sediment. Res.*, 69(2), 338–350.

Wray, J. J., et al. (2011), Columbus crater and other possible groundwater-fed paleolakes of Terra Sirenum, Mars, *J. Geophys. Res.*, 116, E01001, doi:10.1029/2010JE003694.